Supporting Information

A Non-Equilibrium Molecular Dynamics Study of Infra-red Perturbed Electron Transfer

Z. Ma,[a] P. Antoniou[b], P. Zhang,[a] S. Skourtis,[b] and D. Beratan,[a, c, d]

[a]Department of Chemistry, Duke University, Durham, North Carolina, 27708, USA

[b]Department of Physics, University of Cyprus, Nicosia, Cyprus

[c]Department of Physics, Duke University, Durham, North Carolina, 27708, USA

[d]Department of Biochemistry, Duke University, Durham, North Carolina, 27710, USA

I. Non-adiabatic ET rate theory in time domain

Non-adiabatic ET rate expression in time domain is written as[1-2]

$$k_{ET}^{eq} = \frac{1}{\hbar^2}\int dt\, e^{-i\frac{\Delta G}{\hbar}t} C_{H_{DA}}^{eq}(t) C_{FC}^{eq}(t) \tag{S1}$$

ΔG is the reaction free energy, $C_{H_{DA}}^{eq}(t)$ is the donor-acceptor (DA) coupling correlation function in thermal equilibrium (hence the superscript "eq"), $C_{FC}^{eq}(t)$ is the DA energy gap correlation function in thermal equilibrium. In general, DA energy gap correlation function

$$\mathrm{C_{FC}}(t) = \sum_{\nu}\sum_{\mu} P_\nu S_{\nu\mu} \exp\left[\frac{i}{\hbar}(E_\nu - E_\mu)t\right] \tag{S2}$$

and $\mathrm{C_{H_{DA}}}(t)$

$$\mathrm{C_{H_{DA}}}(t) = \sum_{a} P_a \langle a|\hat{H}_{DA}(t)\hat{H}_{DA}(0)|a\rangle \tag{S3}$$

The indices ν and μ denote the quantum number of promoting modes, while a and b denote the inducing modes quantum number, respectively. $|\nu\rangle$ and $|a\rangle$ denote the vibrational wavefunctions of the two types of modes, respectively. $\hat{H}$ is the electronic Hamiltonian. P_ν and P_a are the initial populations of these two types modes, respectively. $S_{\nu\mu} = |\langle\nu|\mu\rangle|^2$ is the Franck-Condon overlap of the promoting mode. $E_{D,\nu,a}$ and $E_{A,\mu,b}$ are the initial and final vibronic state energies, respectively. $\hat{H}_{DA}(t)$ is the time-dependent DA coupling. IR excitation and subsequent IVR produce non-equilibrium population distribution for both the promoting and inducing modes.

II. Time-dependent geometry analysis of DMA-GC-Anth

We identified five H-bond modes that are within IR-excitation frequency range and they all have high computed IR intensity. These modes are illustrated in Fig. 2 of main text. The frequencies and calculated IR intensities of these modes are consistent with the experimental IR spectra as shown below. The DFT computed DMA-GC-Anth vibrational spectrum (unscaled) is plotted in Fig. S0(b) below. They agree closely with the experimental measurements shown in Fig. S0(a). The potential energy changes of the S_2 state along the five selected normal modes (in Fig. 2 of the main text) are also presented in Fig. S0 (c). We find that the potentials are well approximated as being harmonic, thus validating our strategy of analysis.

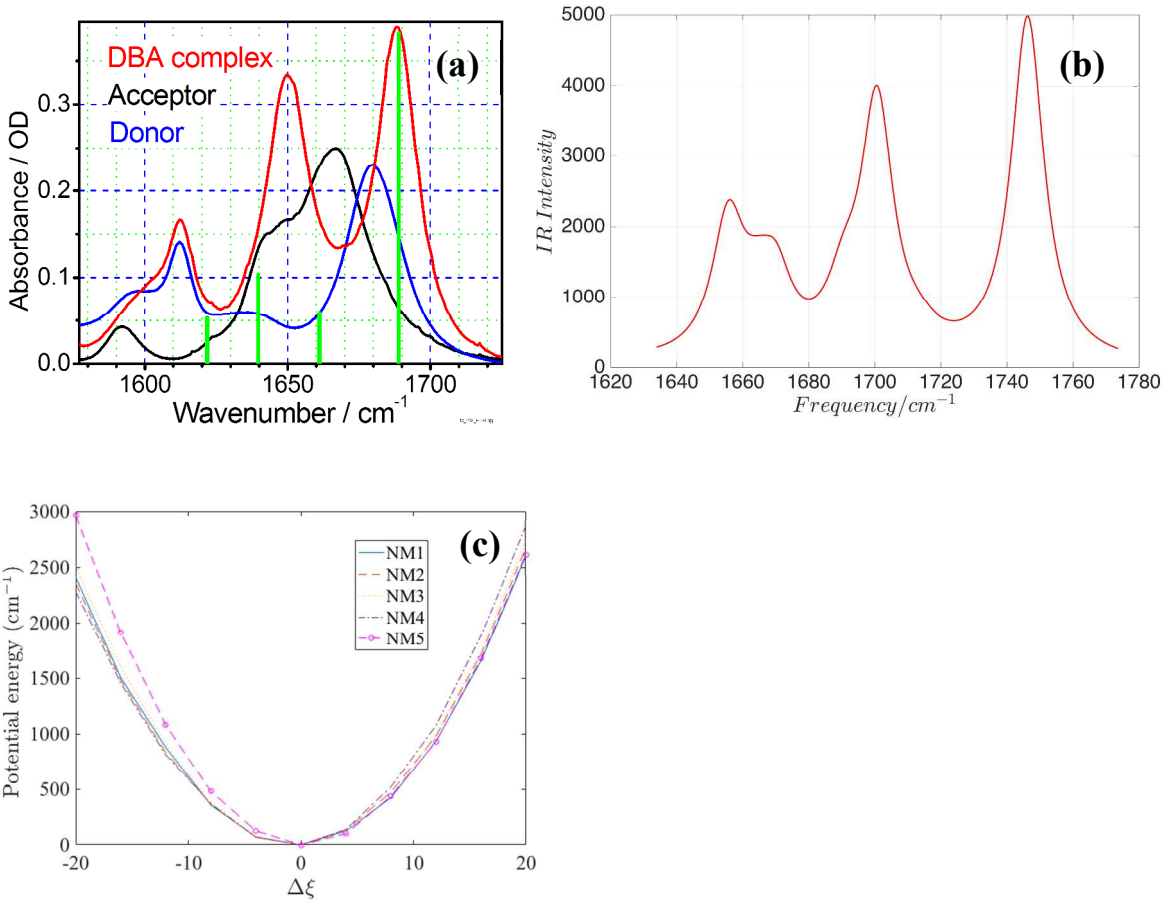

Fig. S0: Measured (a) and computed (b) IR spectra of DMA-GC-Anth. The measured spectra are reproduced from Ref. 5 with permission. (c). Dependence of the TD-B3LYP/6-31G(d,p) computed S_2 state energies of DMA-GC-Anth along the five normal-mode coordinates for IR-active H-bond vibrational modes. The potentials are well approximated as being harmonic. The normal mode notation is given in Fig. 2 of the main text.

II.1. Nuclear motions excited by IR: C=O stretching and H-H-H scissoring

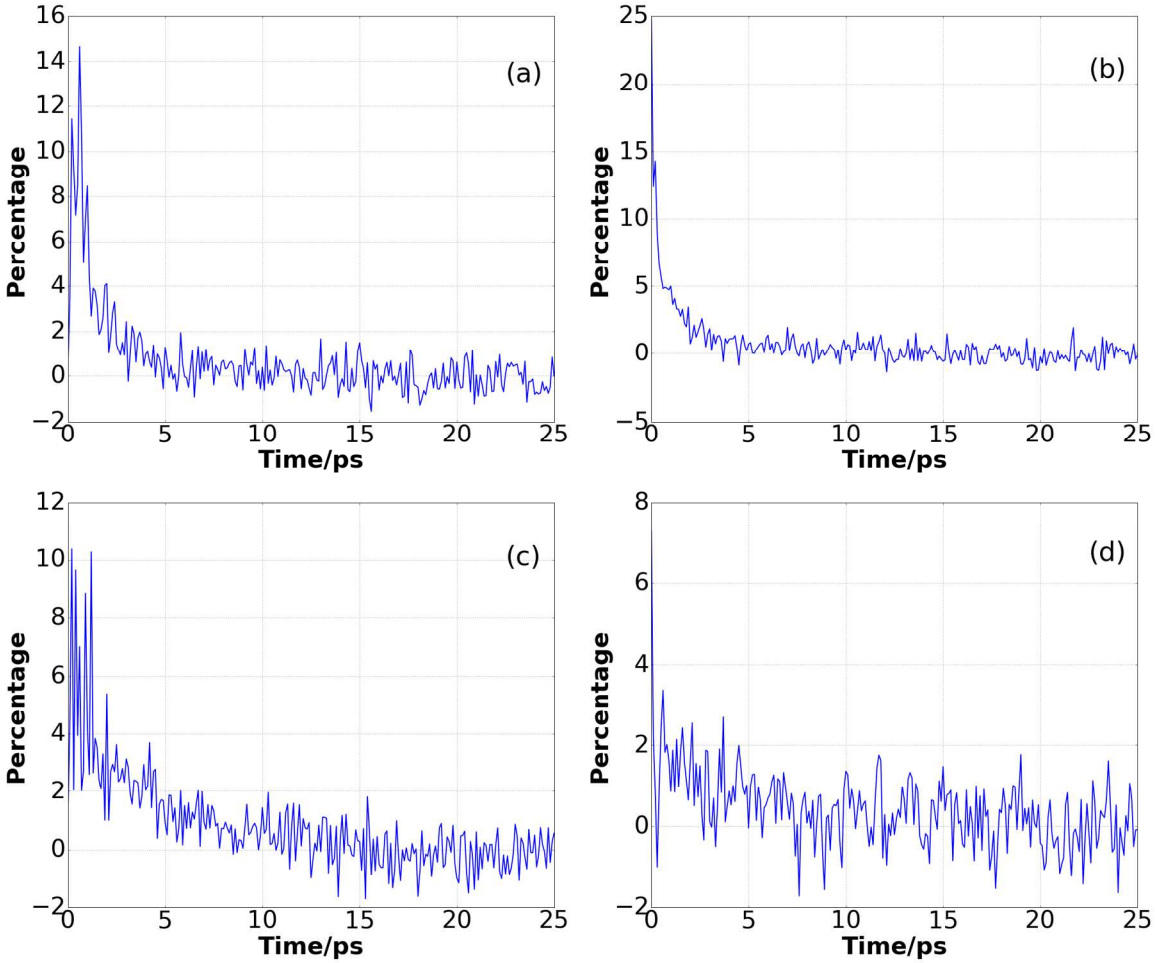

Fig. S1: Time-dependent comparison between the Eq-RMSDs and NEq-RMSDs of: (a) upper left, bond length of the C=O double bond on cytidine fragment; (b) upper right, the H-N-H bond angle of

the NH_2 group on cytidine fragment; (c) bottom left, bond length of the C=O double bond on guanosine fragment; (d) bottom right, the H-N-H bond angle of the NH_2 group on guanosine fragment. For NEq-RMSD, NM2 is excited to its n=1 vibrational state during the non-equilibrium initial condition preparation.

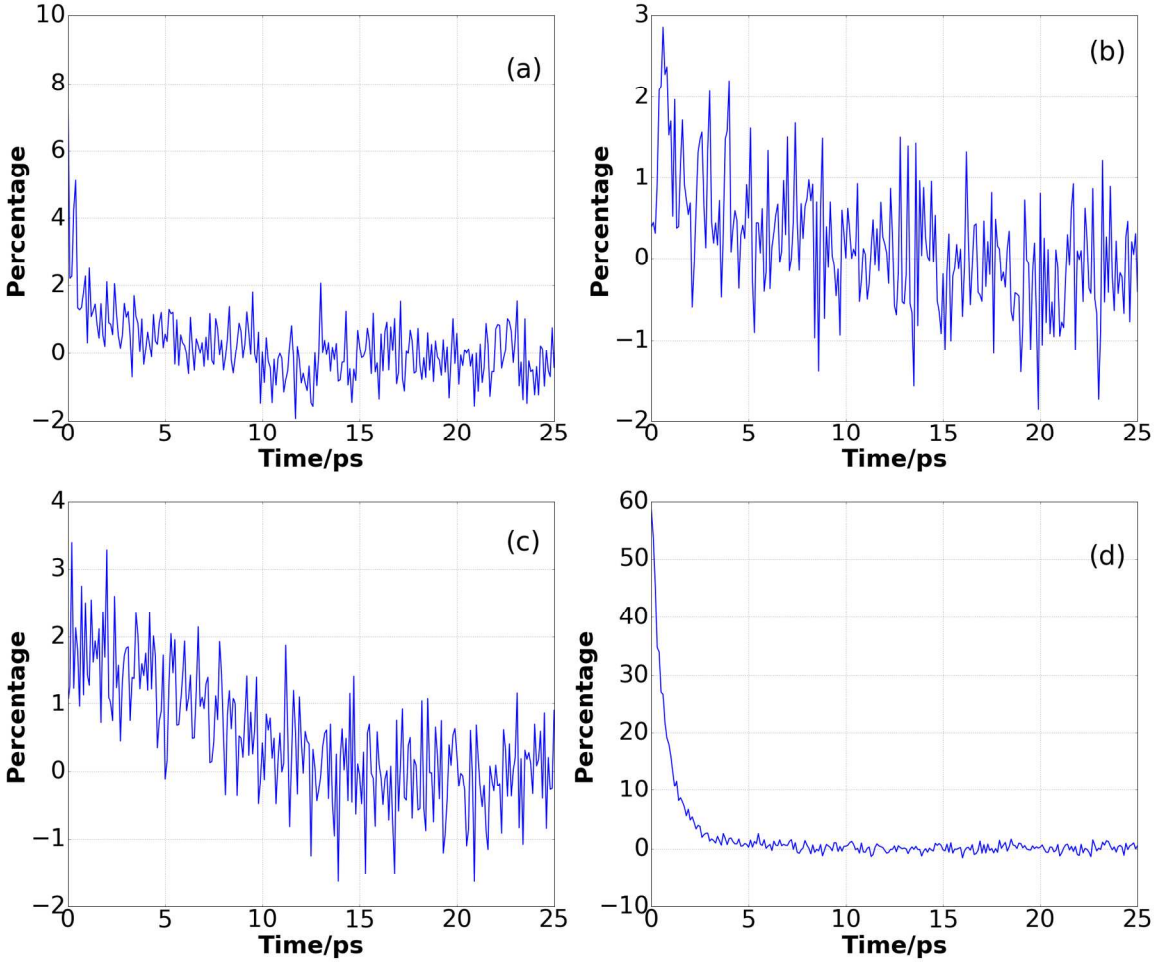

Fig. S2: Time-dependent comparison between the Eq-RMSDs and NEq-RMSDs of: (a) upper left, bond length of the C=O double bond on cytidine fragment; (b) upper right, the H-N-H bond angle of the NH_2 group on cytidine fragment; (c) bottom left, bond length of the C=O double bond on guanosine fragment; (d) bottom right, the H-N-H bond angle of the NH_2 group on guanosine

fragment. For NEq-RMSD, NM3 is excited to its n=1 vibrational state during the non-equilibrium initial condition preparation.

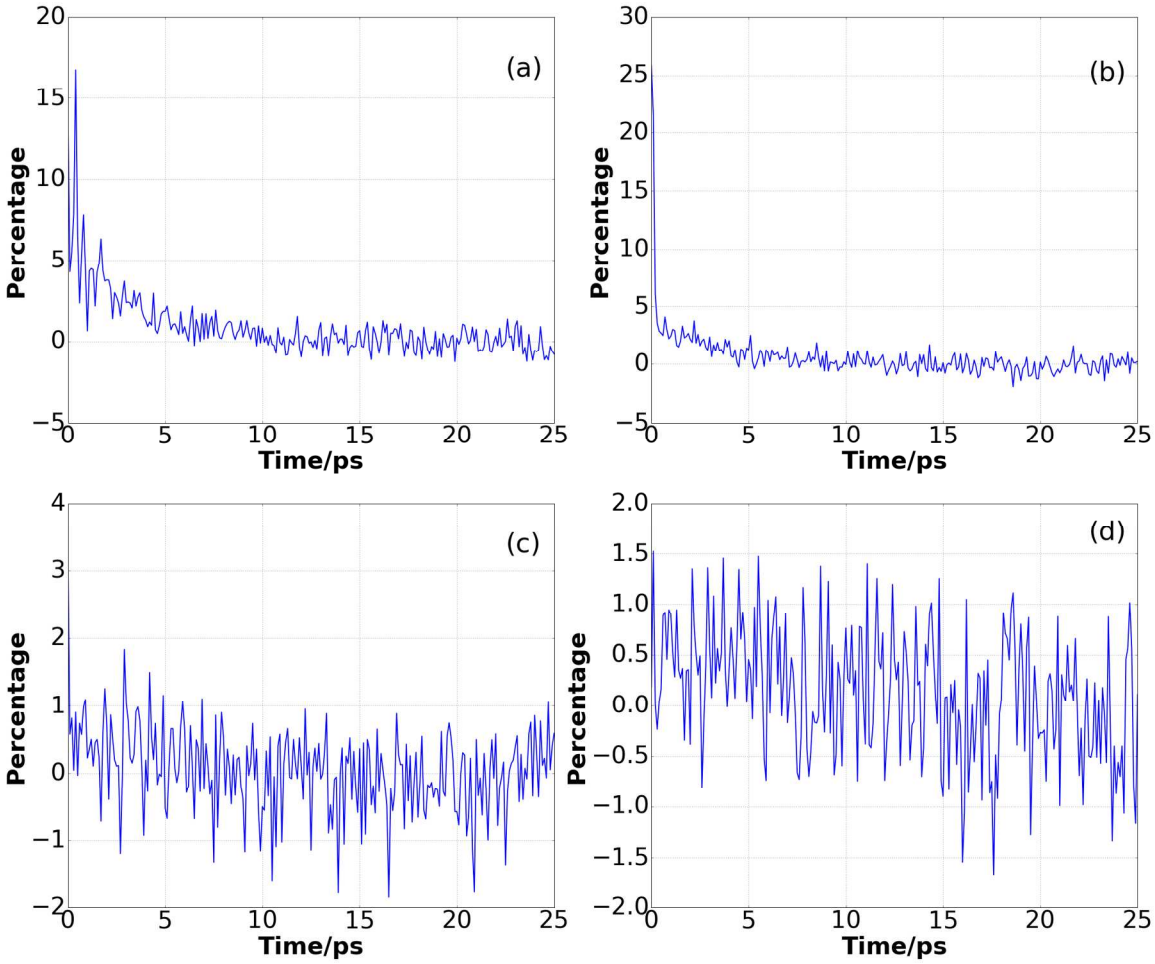

Fig. S3: Time-dependent comparison between the Eq-RMSDs and NEq-RMSDs of: (a) upper left, bond length of the C=O double bond on cytidine fragment; (b) upper right, the H-N-H bond angle of the NH_2 group on cytidine fragment; (c) bottom left, bond length of the C=O double bond on guanosine fragment; (d) bottom right, the H-N-H bond angle of the NH_2 group on guanosine

fragment. For NEq-RMSD, NM4 is excited to its n=1 vibrational state during the non-equilibrium initial condition preparation.

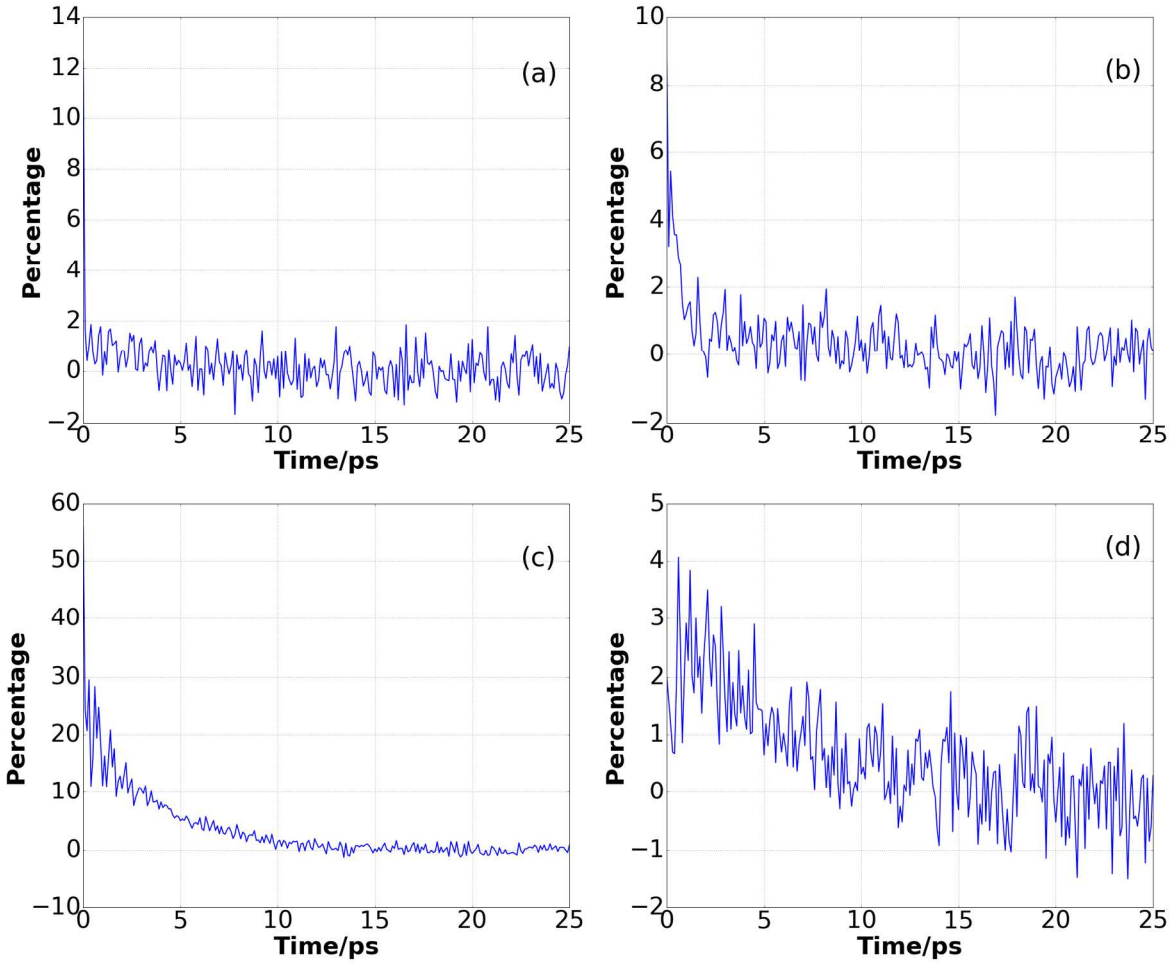

Fig. S4: Time-dependent comparisons between the Eq-RMSDs and NEq-RMSDs of: (a) upper left, bond length of the C=O double bond on cytidine fragment; (b) upper right, the H-N-H bond angle of the NH_2 group on cytidine fragment; (c) bottom left, bond length of the C=O double bond on guanosine fragment; (d) bottom right, the H-N-H bond angle of the NH_2 group on guanosine

fragment. For NEq-RMSD, NM5 is excited to its n=1 vibrational state during the non-equilibrium initial condition preparation.

II.2. Geometry and orientation of guanosine and cytidine fragments

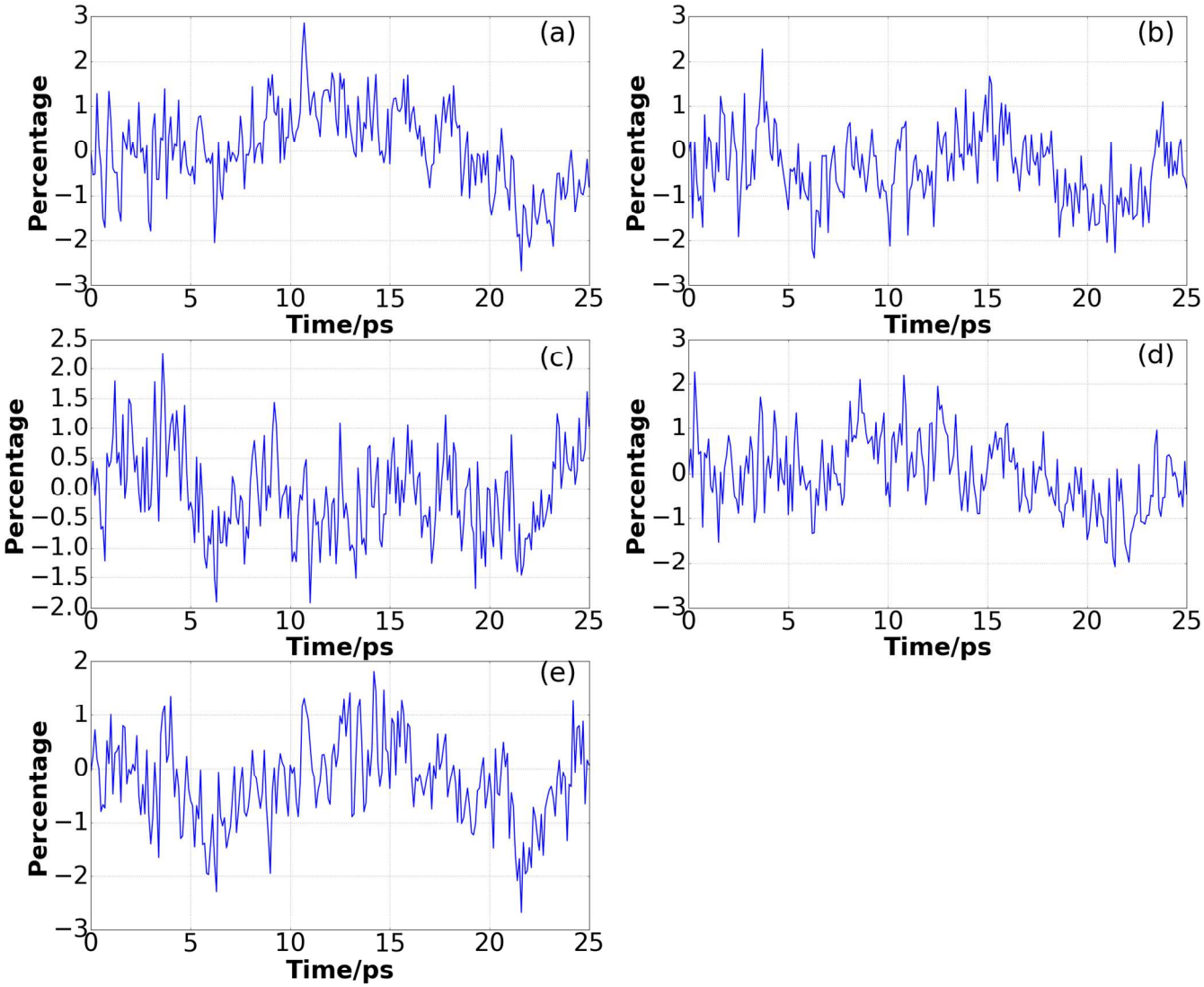

Fig. S5. Time-dependent percentage differences between the Eq-RMSDs and NEq-RMSDs of guanosine-cytidine center-of-mass distances. The NEq-RMSDs are computed using the non-equilibrium ensembles produced by the initial vibrational excitation of (a) NM1; (b) NM2; (c) NM3; (d) NM4 and (e) NM5 in DMA-GC-Anth.

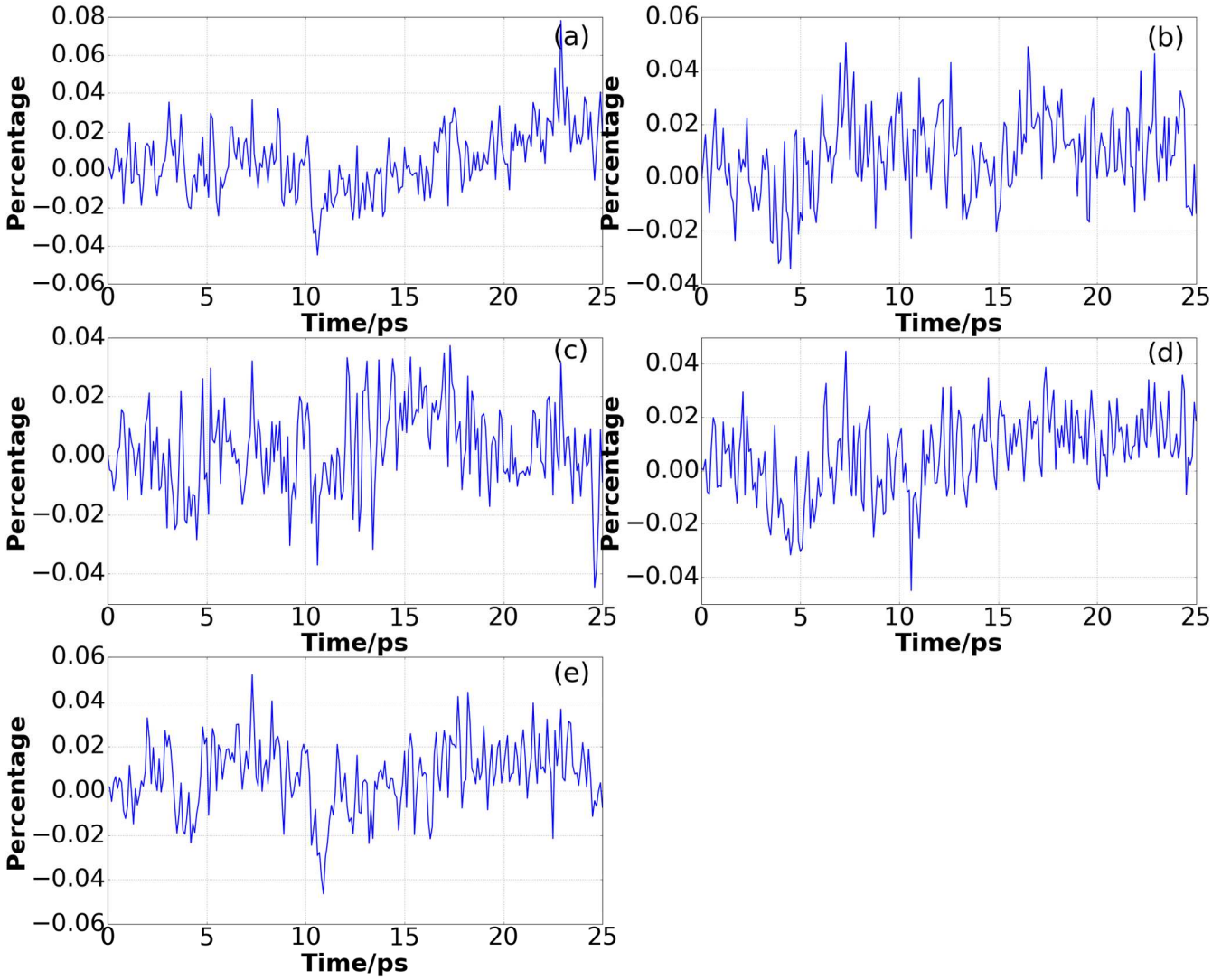

Fig. S6. Time-dependent percentage differences between the Eq-mean and NEq-means of guanosine-cytidine center-of-mass distances. The NEq-means are computed using the non-

equilibrium ensembles produced by the initial vibrational excitation of (a) NM1; (b) NM2; (c) NM3; (d) NM4 and (e) NM5 in DMA-GC-Anth.

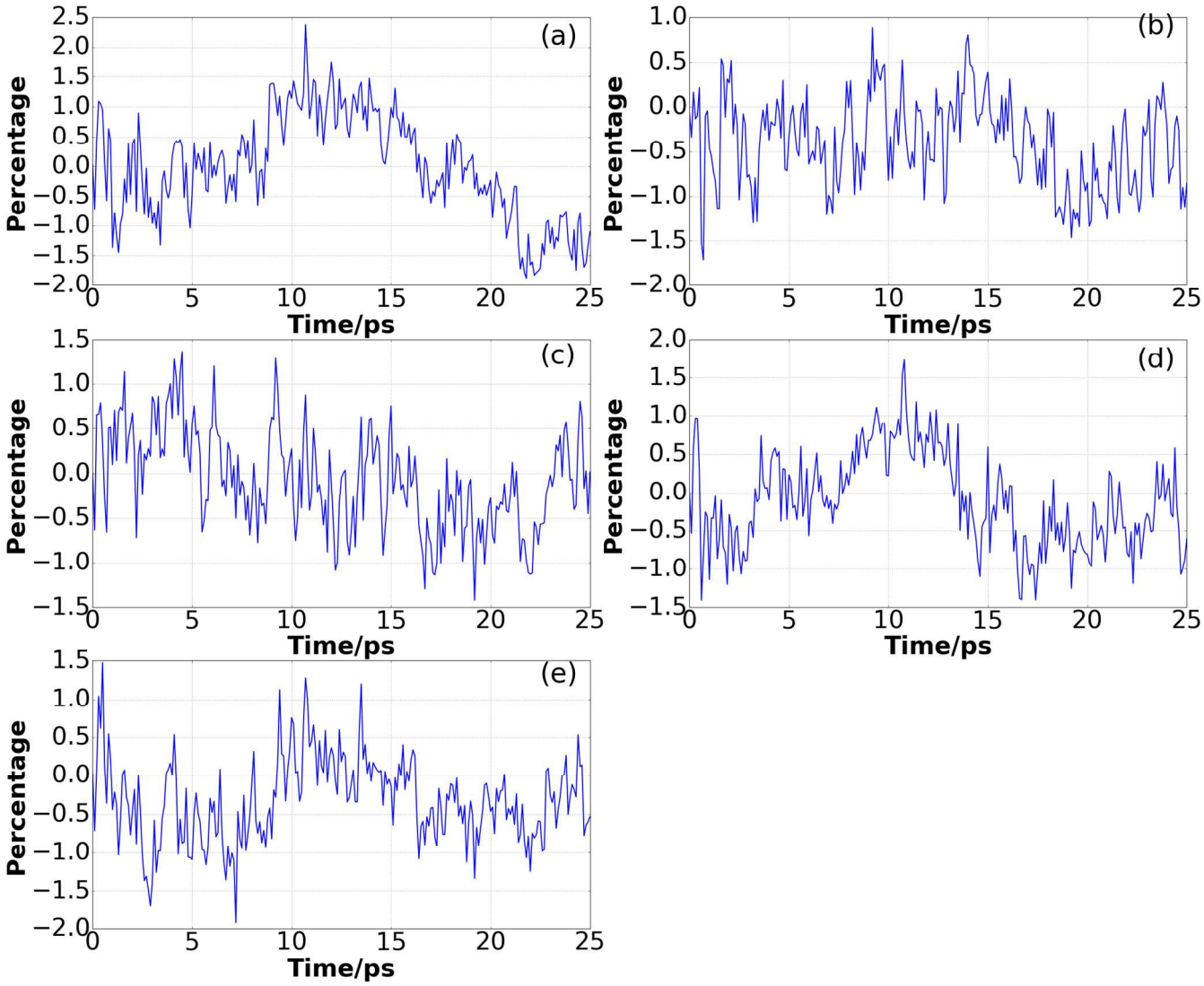

Fig. S7. Time-dependent percentage differences between the Eq-RMSDs and NEq-RMSDs of guanosine-cytidine torsion angle defined by the angle between the normal vectors of guanosine and

cytidine planes. The NEq-RMSDs are computed using the non-equilibrium ensembles produced by the initial vibrational excitation of (a) NM1; (b) NM2; (c) NM3; (d) NM4 and (e) NM5 in DMA-GC-Anth.

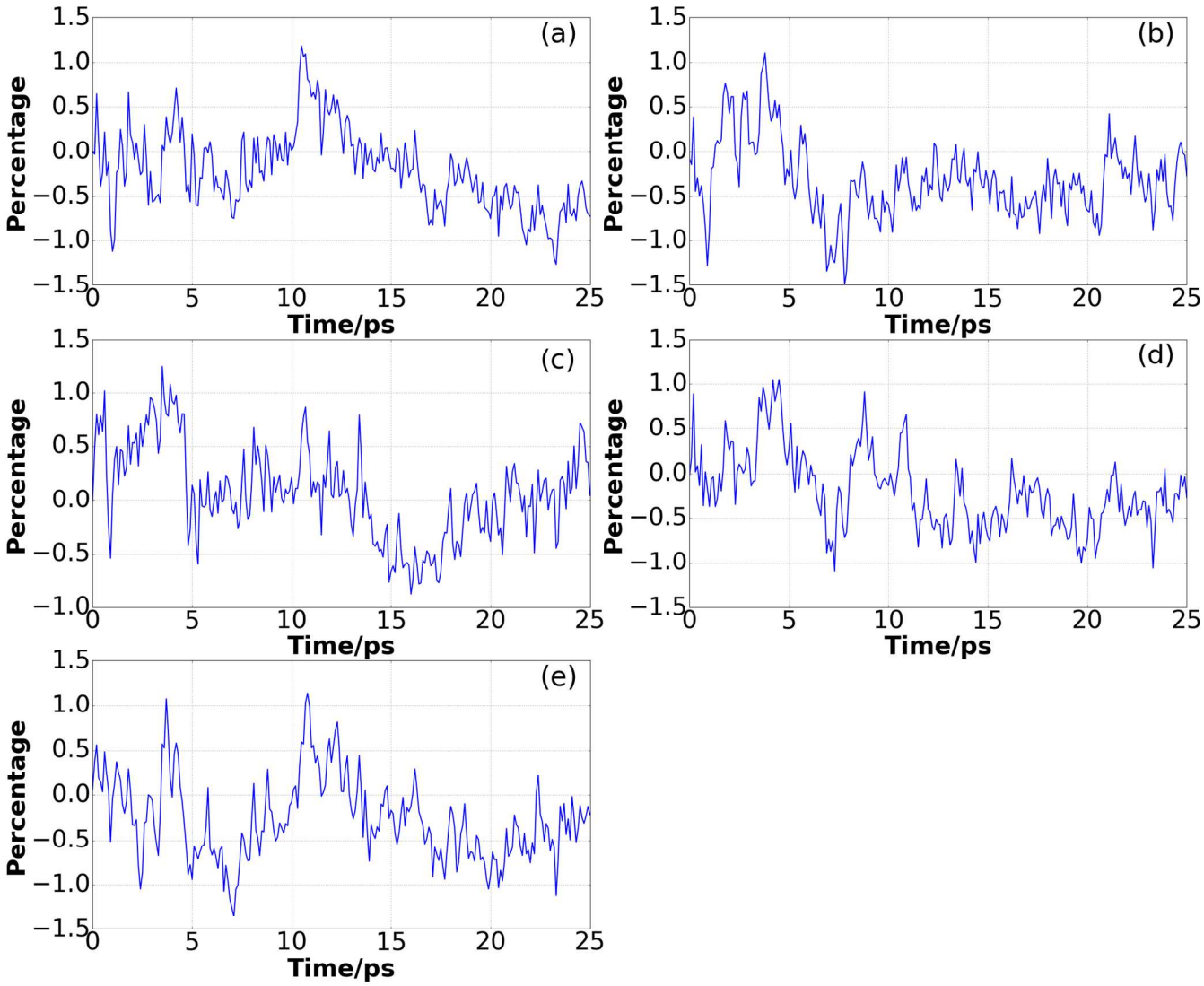

Fig. S8. Time-dependent percentage differences between the Eq-mean and NEq-means of guanosine-cytidine torsion angle defined by the angle between the normal vectors of guanosine and

cytidine planes. The NEq-means are computed using the non-equilibrium ensembles produced by the initial vibrational excitation of (a) NM1; (b) NM2; (c) NM3; (d) NM4 and (e) NM5 in DMA-GC-Anth.

II.3 Hydrogen bonding in-plane geometry

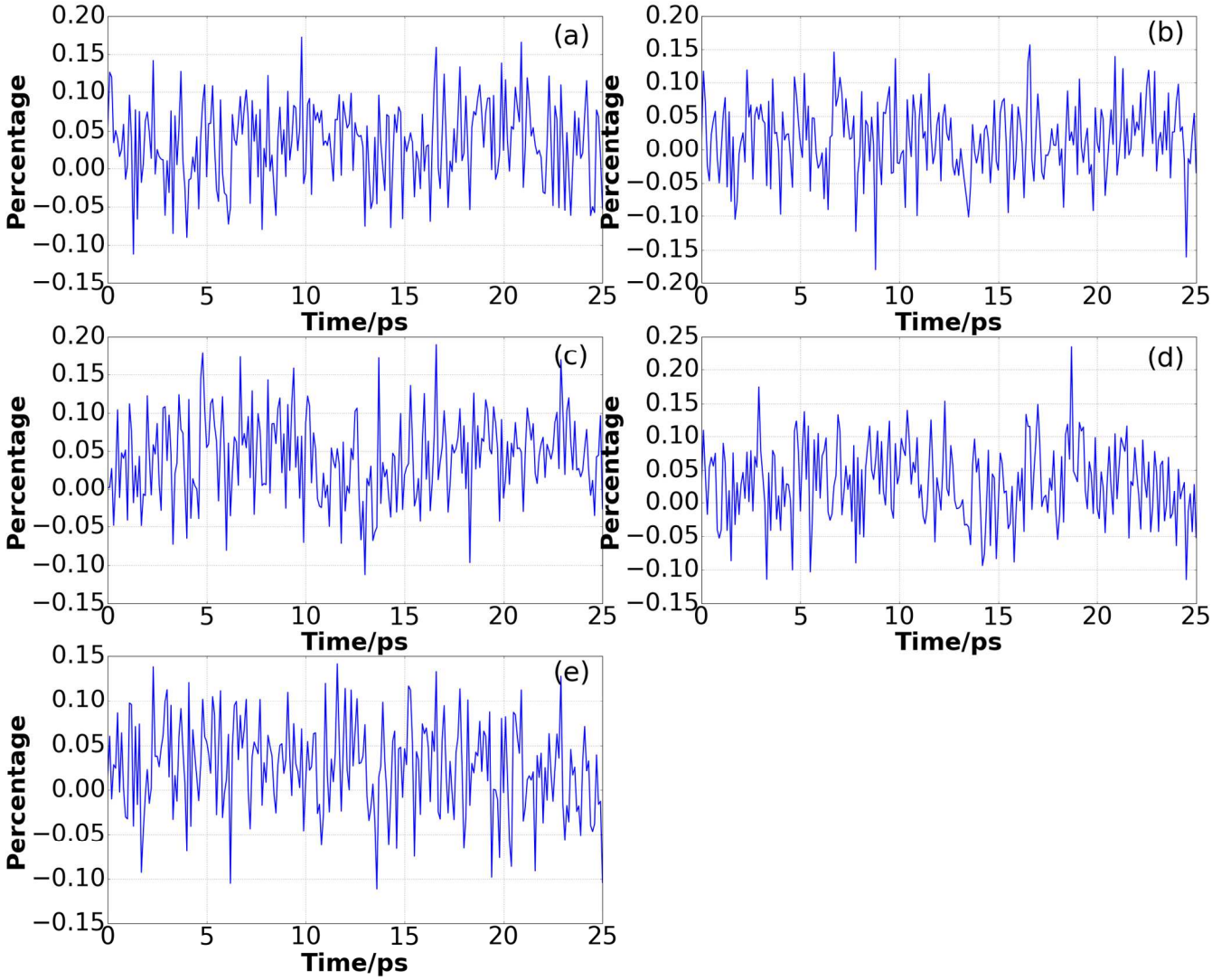

Fig. S9. Time-dependent percentage differences between the Eq-means and NEq-means of the first H-bond length. The NEq-means are computed using the non-equilibrium ensembles produced by the initial vibrational excitation of (a) NM1; (b) NM2; (c) NM3; (d) NM4 and (e) NM5 in DMA-GC-Anth.

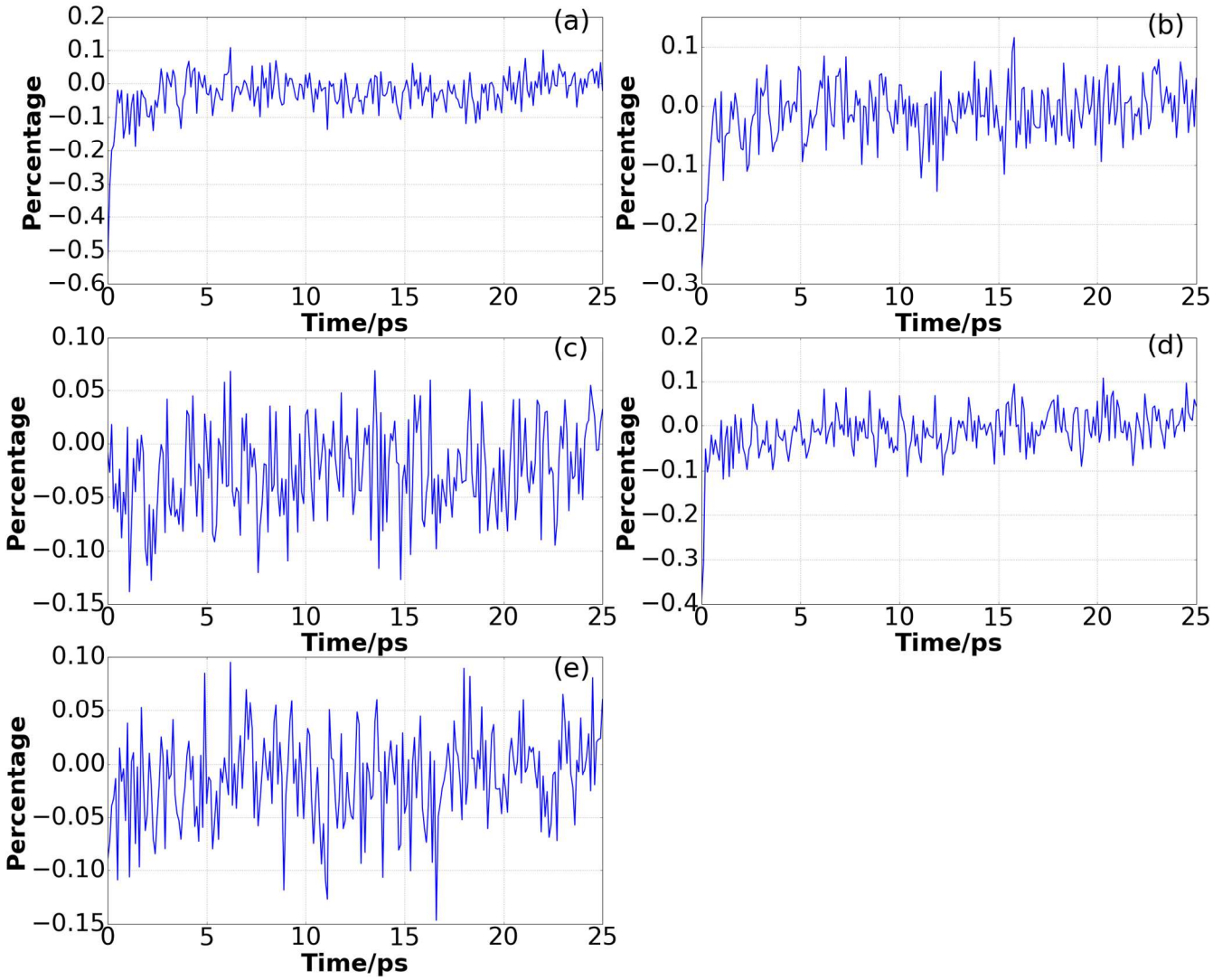

Fig. S10. Time-dependent percentage differences between the Eq-means and NEq-means of the first H-bond angle. The NEq-means are computed using the non-equilibrium ensemble produced by the

initial vibrational excitation of (a) NM1; (b) NM2; (c) NM3; (d) NM4 and (e) NM5 in DMA-GC-Anth.

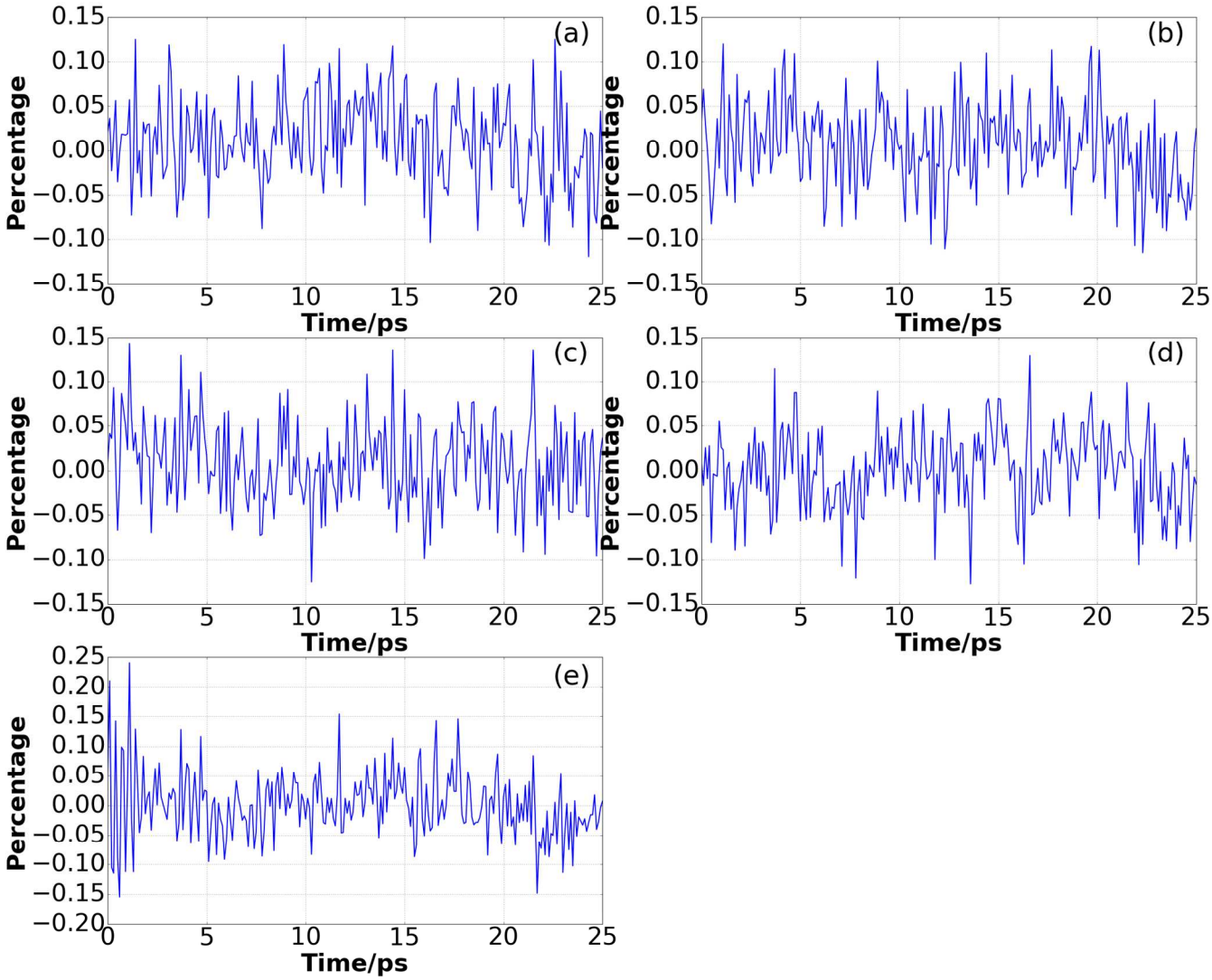

Fig. S11. Time-dependent percentage differences between the Eq-means and NEq-means of the second H-bond length. The NEq-means are computed using the non-equilibrium ensembles

produced by the initial vibrational excitation of (a) NM1; (b) NM2; (c) NM3; (d) NM4 and (e) NM5 in DMA-GC-Anth.

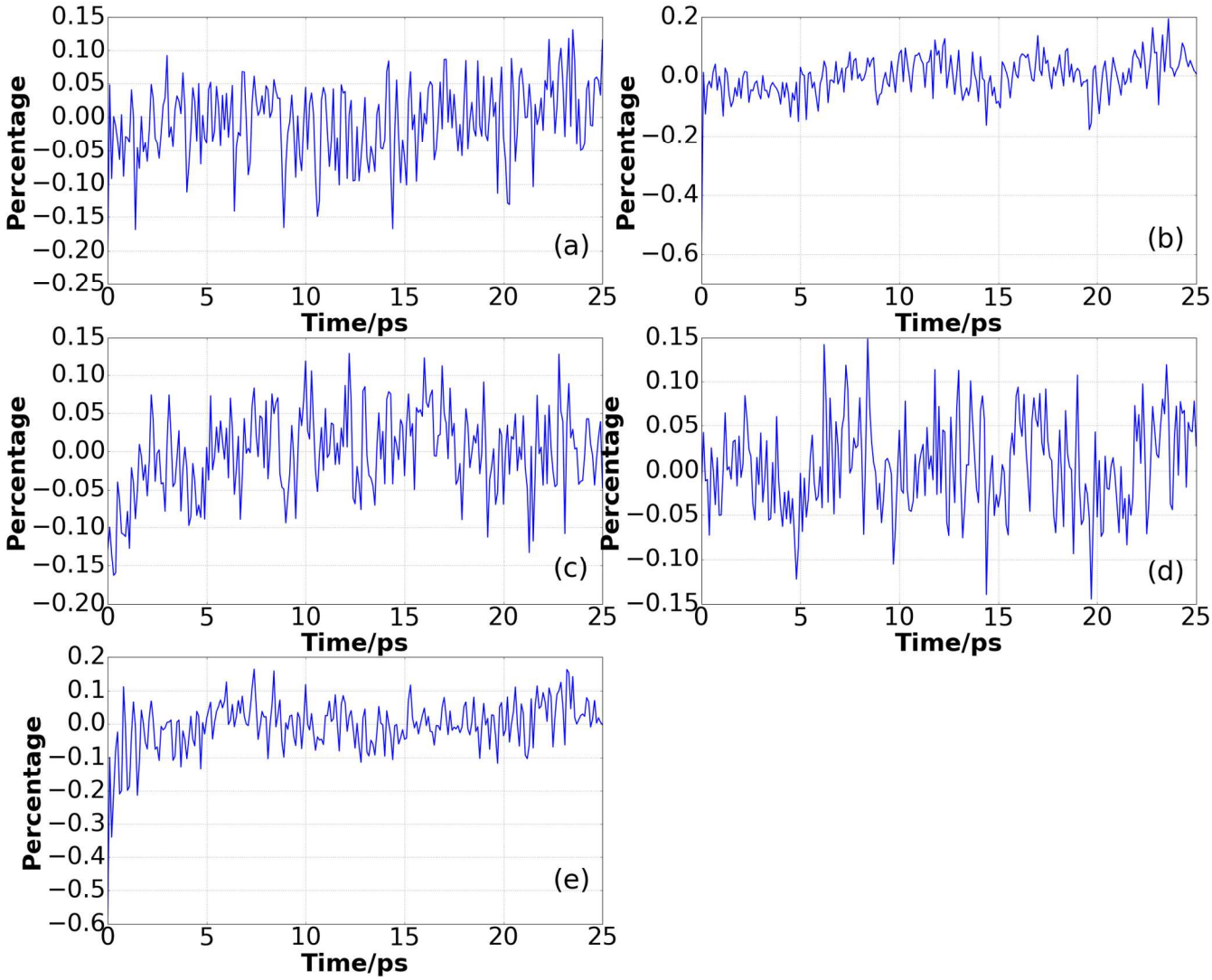

Fig. S12. Time-dependent percentage differences between the Eq-means and NEq-means of the second H-bond angle. The NEq-means are computed using the non-equilibrium ensembles produced

by the initial vibrational excitation of (a) NM1; (b) NM2; (c) NM3; (d) NM4 and (e) NM5 in DMA-GC-Anth.

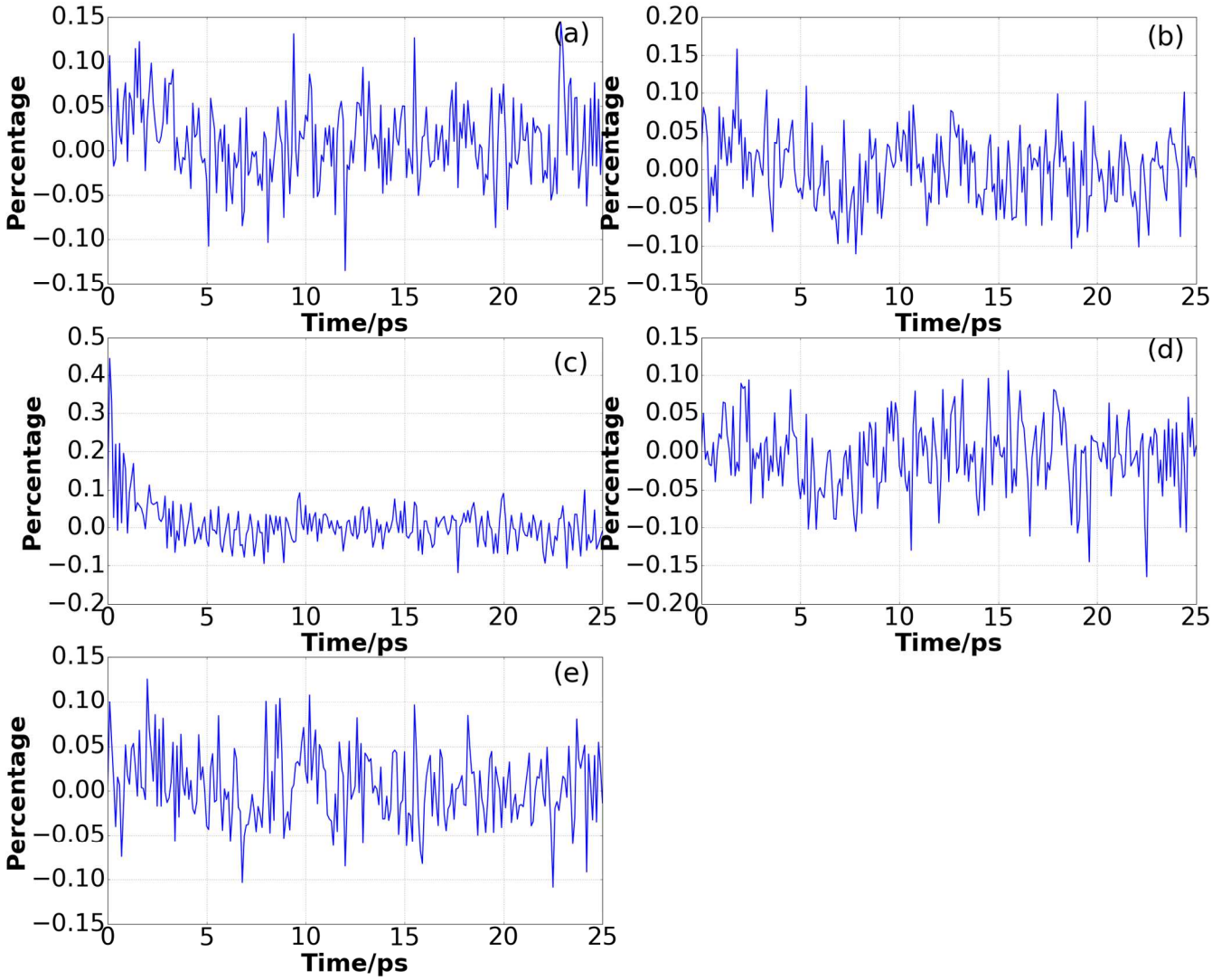

Fig. S13. Time-dependent percentage differences between the Eq-means and NEq-means of the third H-bond length. The NEq-means are computed using the non-equilibrium ensembles produced by the

initial vibrational excitation of (a) NM1; (b) NM2; (c) NM3; (d) NM4 and (e) NM5 in DMA-GC-Anth.

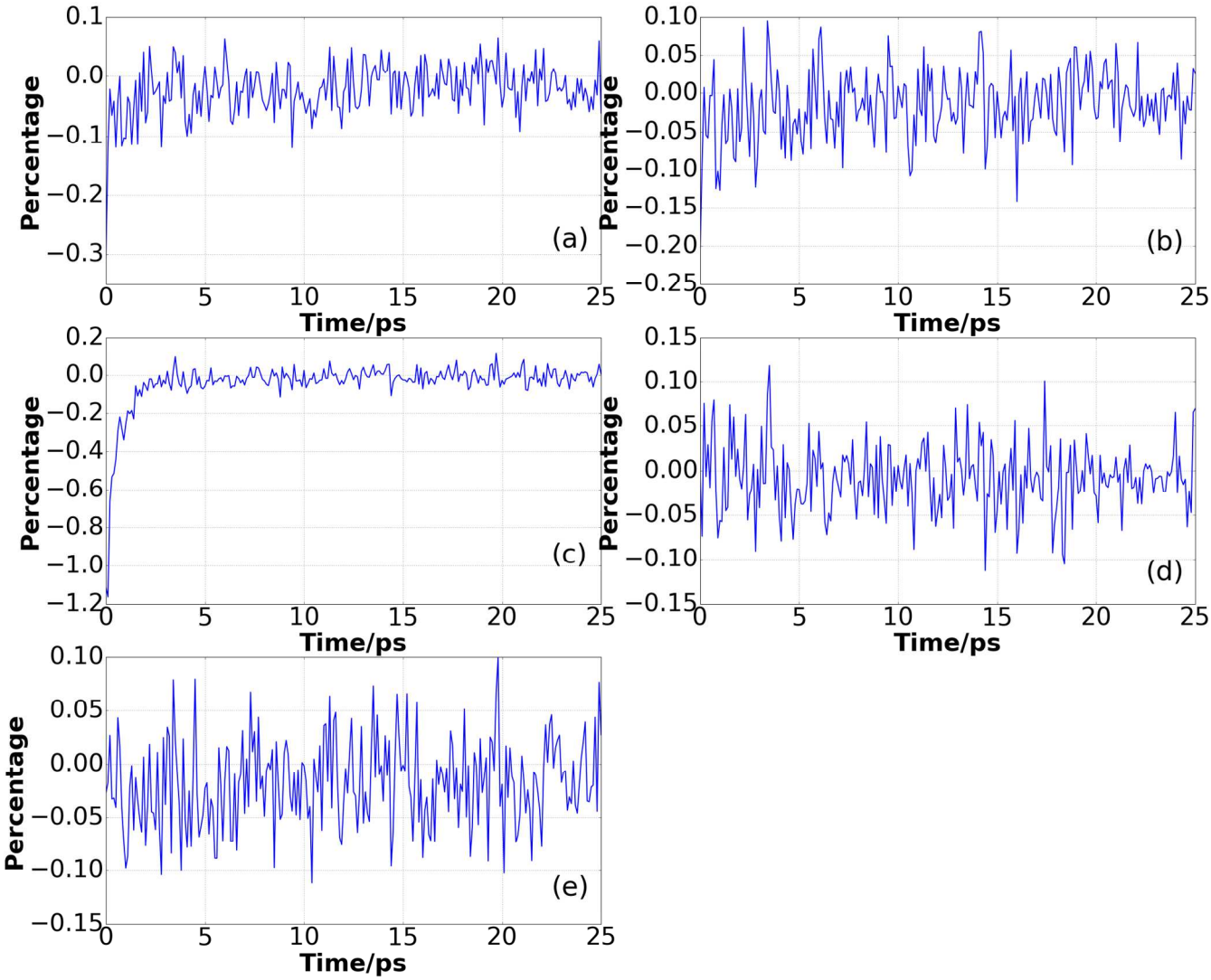

Fig. S14. Time-dependent percentage differences between the Eq-means and NEq-means of the third H-bond angle. The NEq-means are computed using the non-equilibrium ensembles produced by the

initial vibrational excitation of (a) NM1; (b) NM2; (c) NM3; (d) NM4 and (e) NM5 in DMA-GC-Anth.

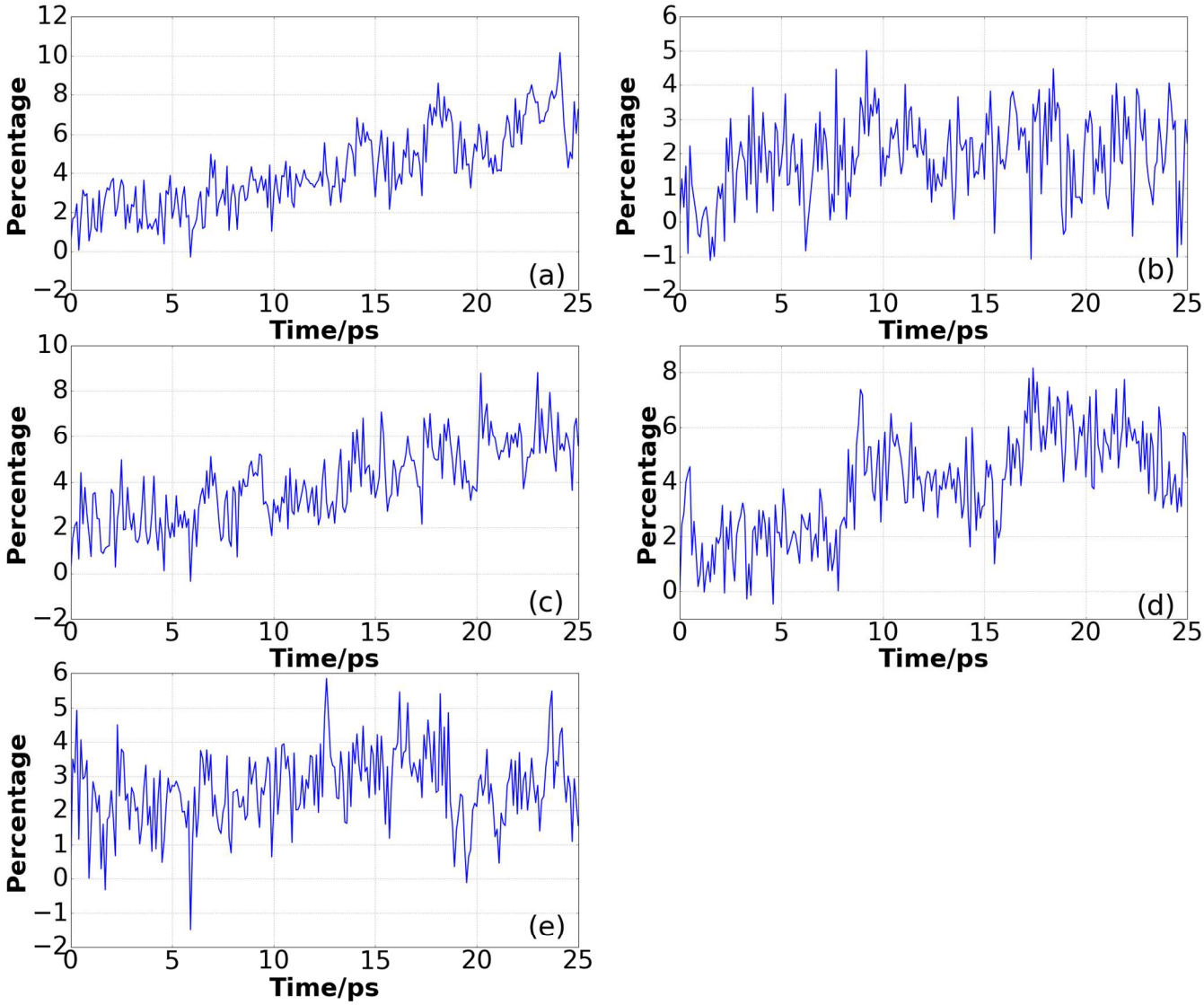

Fig. S15. Time-dependent percentage differences between the Eq-RMSDs and NEq-RMSDs of the first H-bond length. The NEq-RMSDs are computed using the non-equilibrium ensembles produced by the initial vibrational excitation of (a) NM1; (b) NM2; (c) NM3; (d) NM4 and (e) NM5 in DMA-GC-Anth.

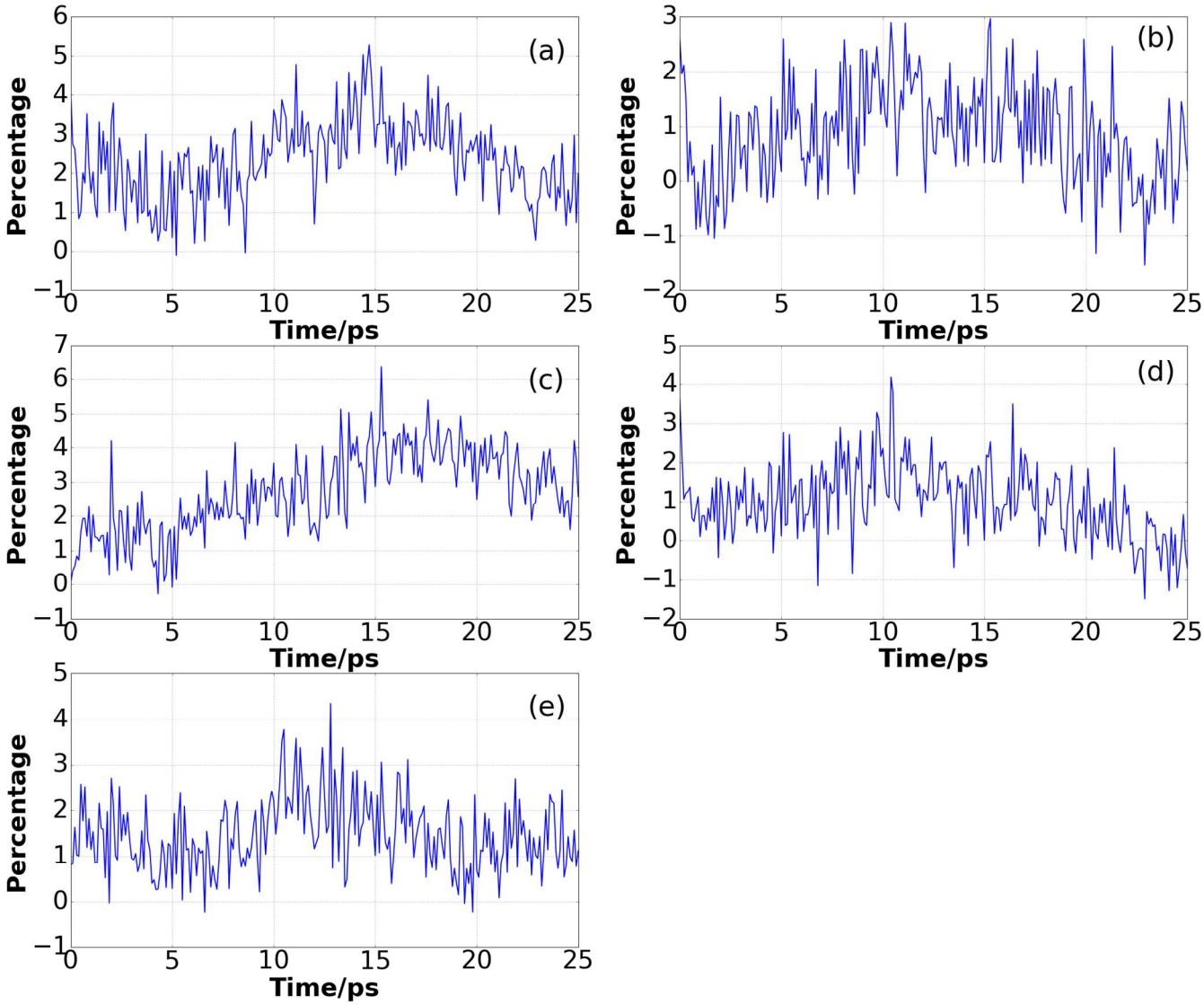

Fig. S16. Time-dependent percentage differences between the Eq-RMSDs and NEq-RMSDs of the first H-bond angle. The NEq-RMSDs are computed using the non-equilibrium ensembles produced by the initial vibrational excitation of (a) NM1; (b) NM2; (c) NM3; (d) NM4 and (e) NM5 in DMA-GC-Anth.

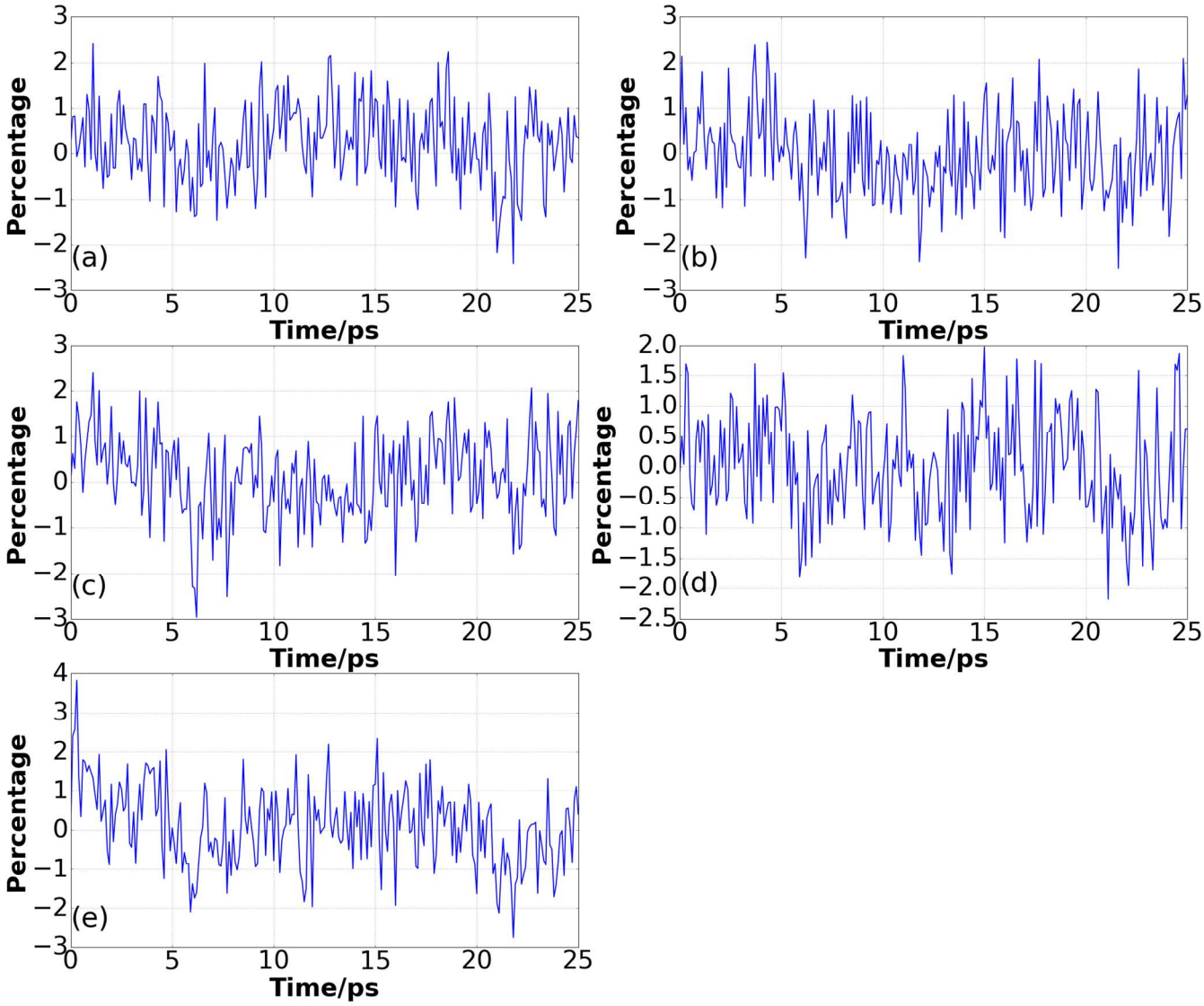

Fig. S17. Time-dependent percentage differences between the Eq-RMSDs and NEq-RMSDs of the second H-bond length. The NEq-RMSDs are computed using the non-equilibrium ensembles produced by the initial vibrational excitation of (a) NM1; (b) NM2; (c) NM3; (d) NM4 and (e) NM5 in DMA-GC-Anth.

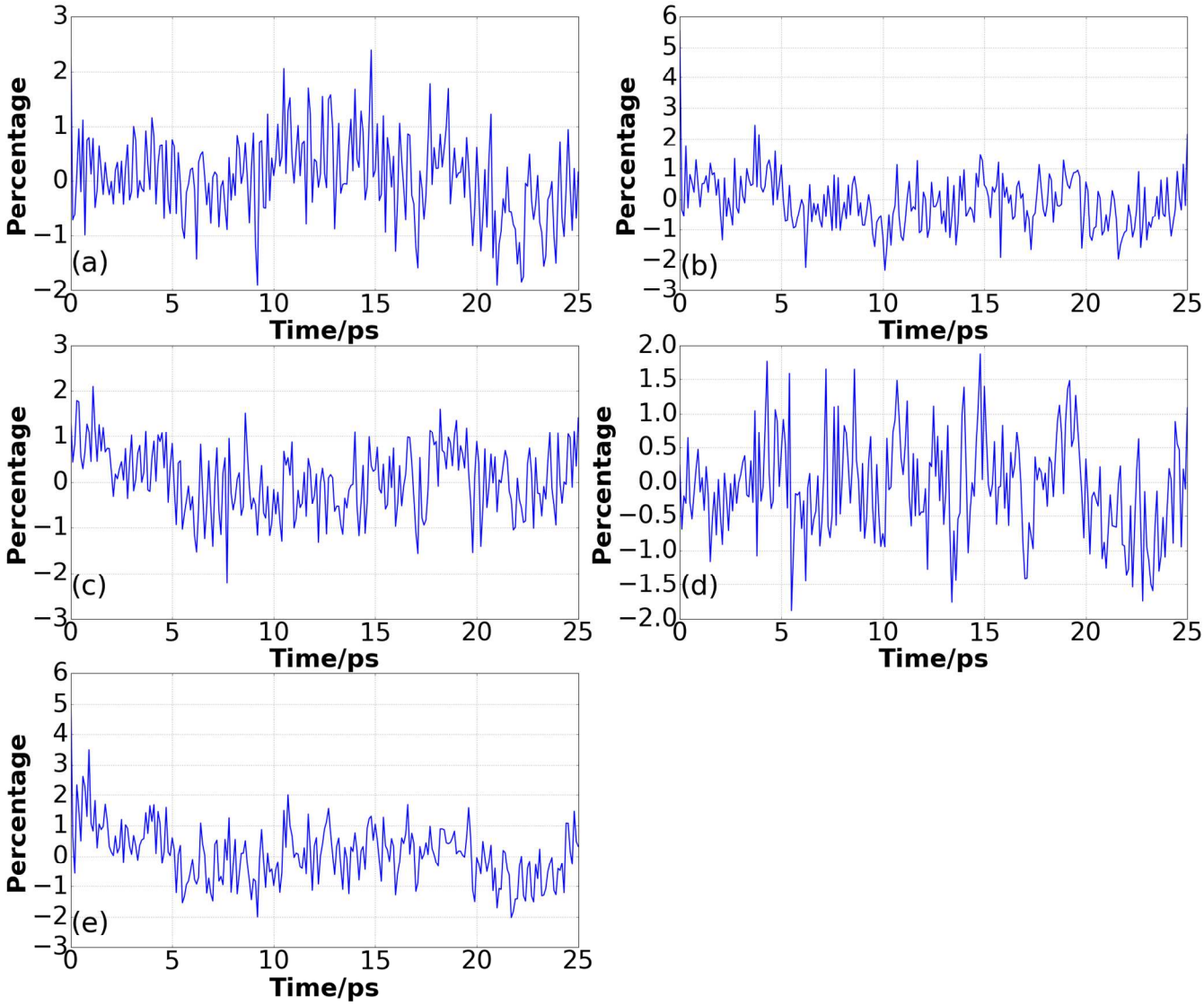

Fig. S18. Time-dependent percentage differences between the Eq-RMSDs and NEq-RMSDs of the second H-bond angle. The NEq-RMSDs are computed using the non-equilibrium ensembles produced by the initial vibrational excitation of (a) NM1; (b) NM2; (c) NM3; (d) NM4 and (e) NM5 in DMA-GC-Anth.

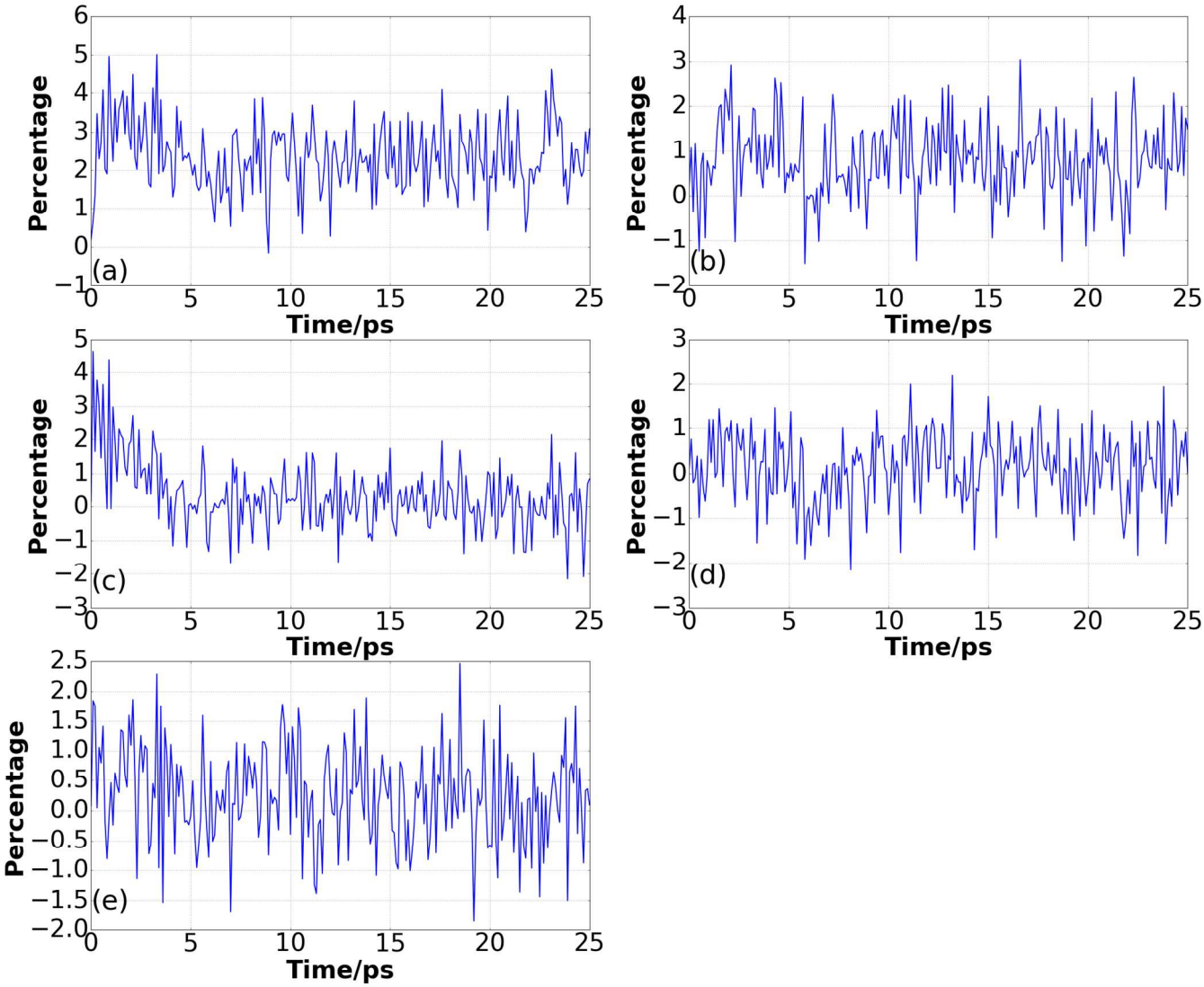

Fig. S19. Time-dependent percentage differences between the Eq-RMSDs and NEq-RMSDs of the third H-bond length. The NEq-RMSDs are computed using the non-equilibrium ensembles produced by the initial vibrational excitation of (a) NM1; (b) NM2; (c) NM3; (d) NM4 and (e) NM5 in DMA-GC-Anth.

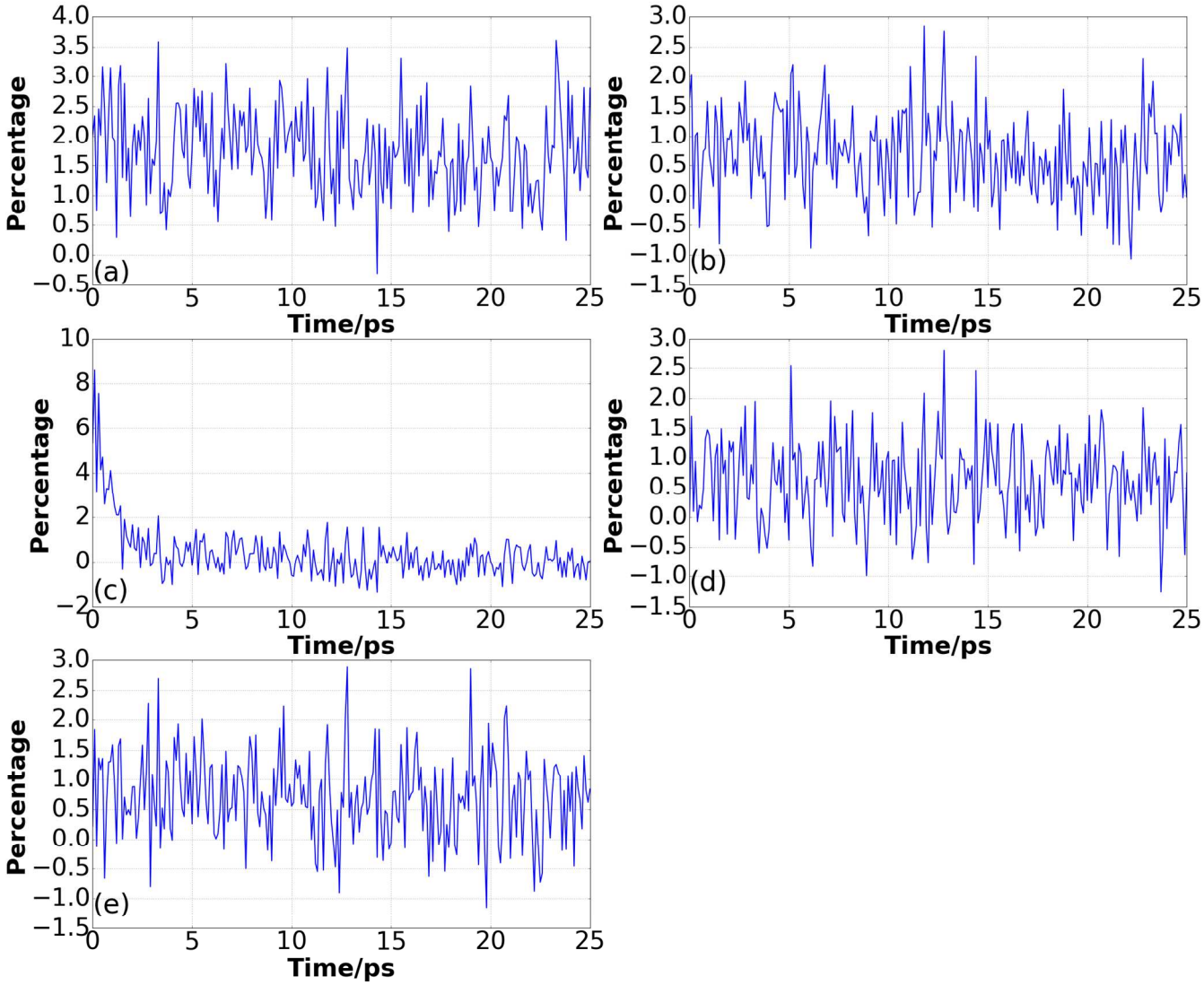

Fig. S20. Time-dependent percentage differences between the Eq-RMSDs and NEq-RMSDs of the third H-bond angle. The NEq-RMSDs are computed using the non-equilibrium ensembles produced by the initial vibrational excitation of (a) NM1; (b) NM2; (c) NM3; (d) NM4 and (e) NM5 in DMA-GC-Anth.

II.4 Hydrogen bonds out-of-plane geometry

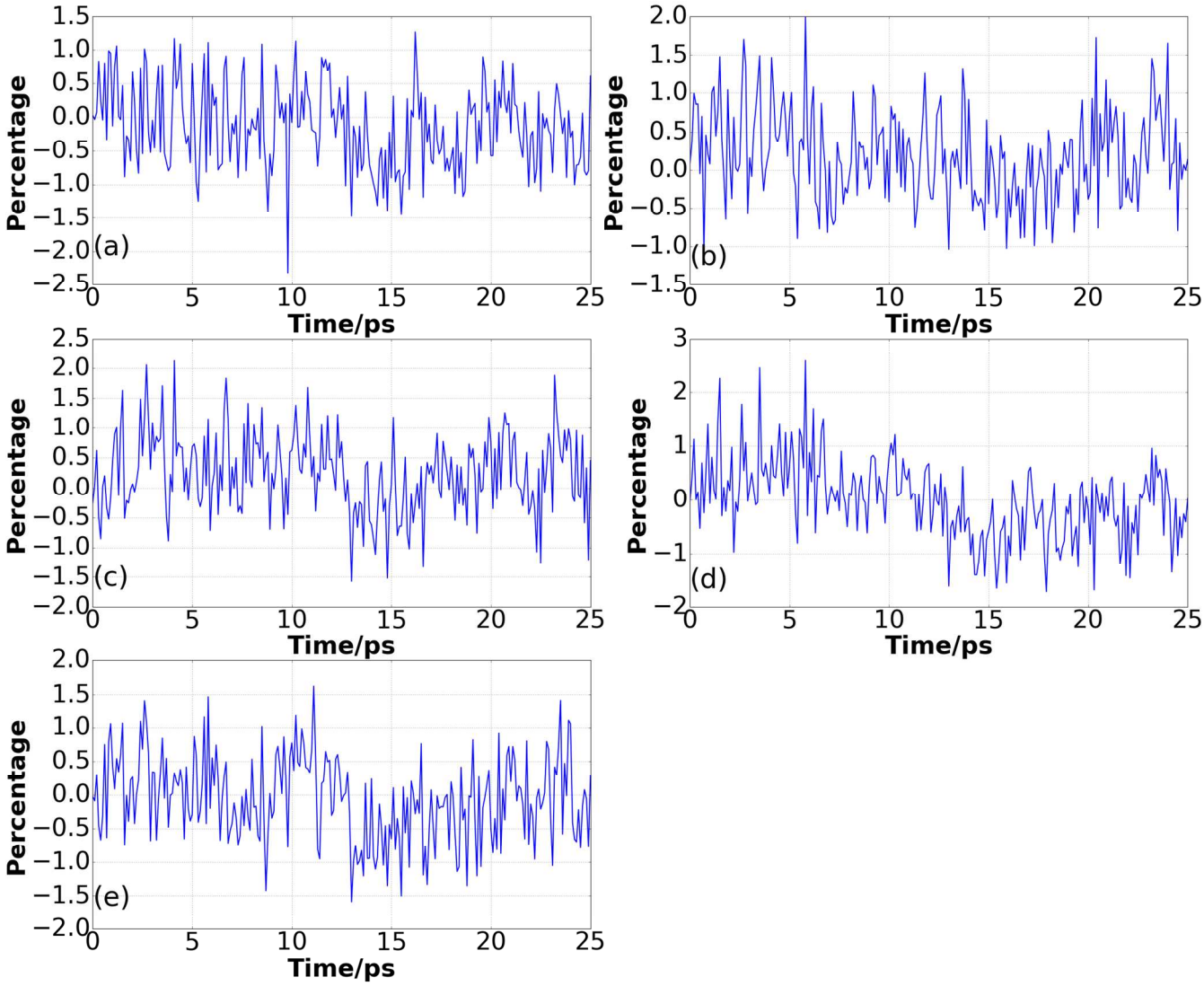

Fig. S21. Time-dependent percentage differences between the Eq-means and NEq-means of the vertical distance between the cytidine plane and the hydrogen atom in the first H-bond. The NEq-means are computed using the non-equilibrium ensembles produced by the initial vibrational excitation of (a) NM1; (b) NM2; (c) NM3; (d) NM4 and (e) NM5 in DMA-GC-Anth.

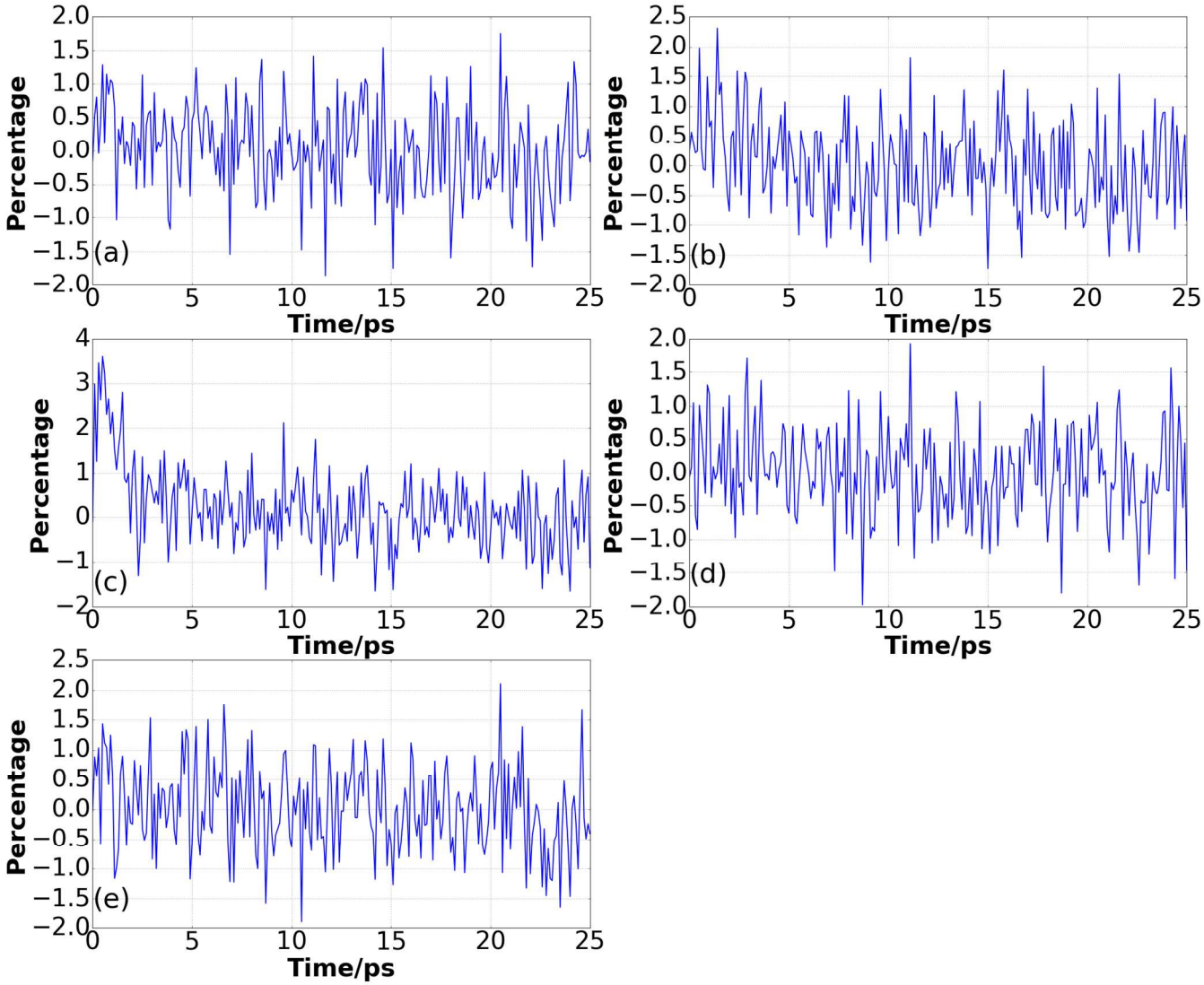

Fig. S22. Time-dependent percentage differences between the Eq-means and NEq-means of the vertical distance between the guanosine plane and the hydrogen atom in the second H-bond. The NEq-means are computed using the non-equilibrium ensembles produced by the initial vibrational excitation of (a) NM1; (b) NM2; (c) NM3; (d) NM4 and (e) NM5 in DMA-GC-Anth.

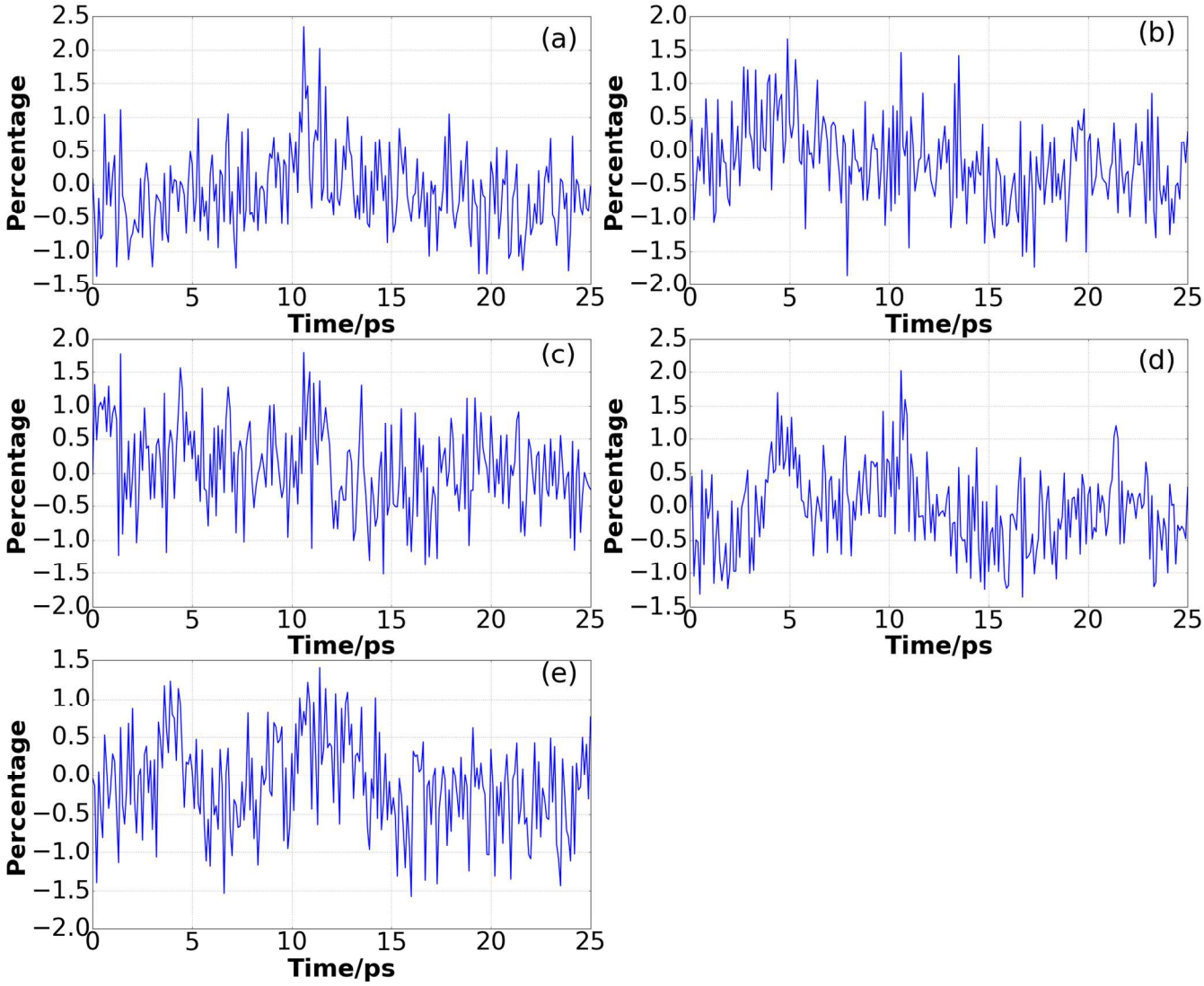

Fig. S23. Time-dependent percentage differences between the Eq-means and NEq-means of the vertical distance between the guanosine plane and the hydrogen atom in the third H-bond. The NEq-means are computed using the non-equilibrium ensemble produced by the initial vibrational excitation of (a) NM1; (b) NM2; (c) NM3; (d) NM4 and (e) NM5 in DMA-GC-Anth.

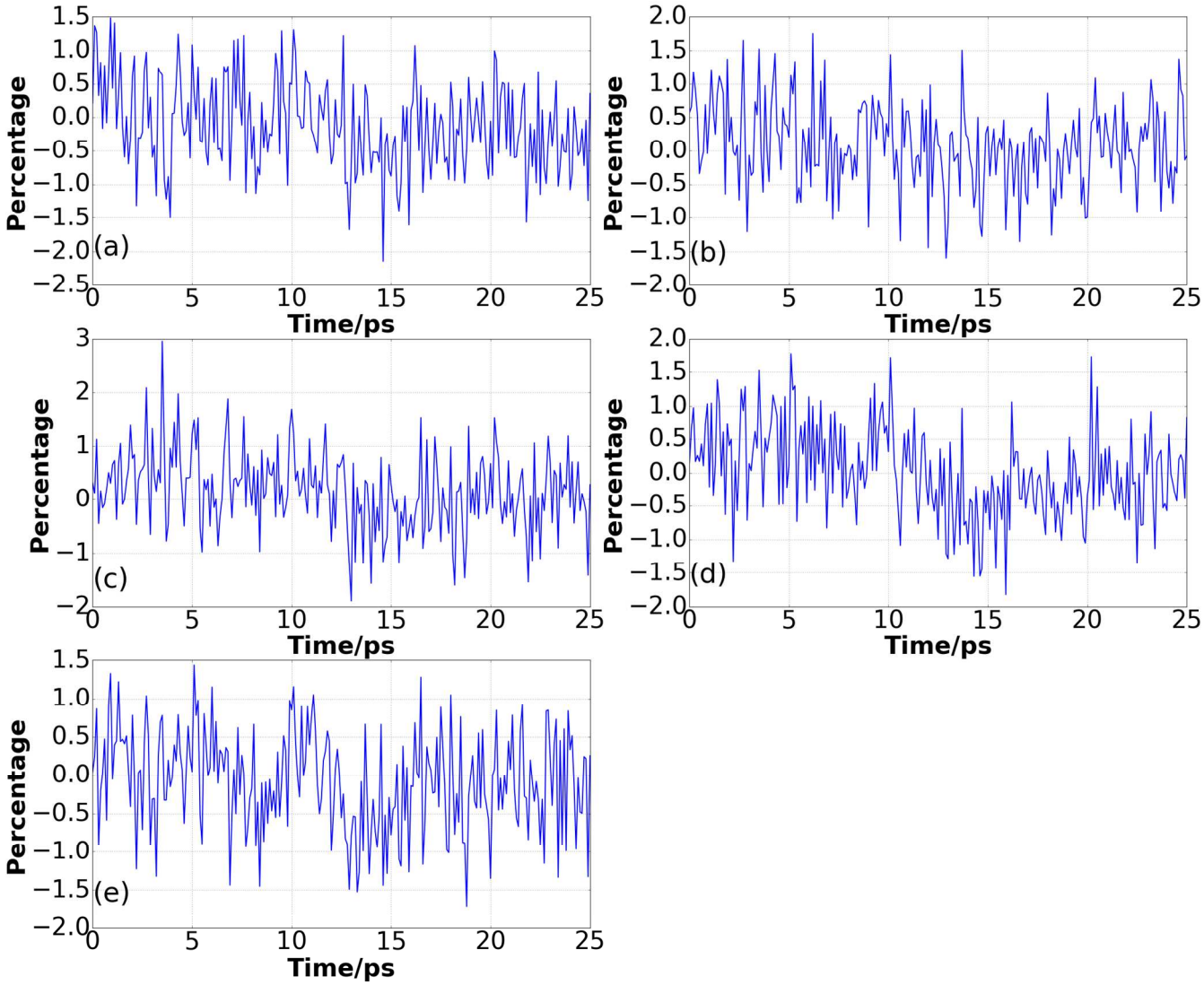

Fig. S24. Time-dependent percentage differences between the Eq-RMSDs and NEq-RMSDs of the vertical distance between the cytidine plane and the hydrogen atom in the first H-bond. The NEq-RMSDs are computed using the non-equilibrium ensembles produced by the initial vibrational excitation of (a) NM1; (b) NM2; (c) NM3; (d) NM4 and (e) NM5 in DMA-GC-Anth.

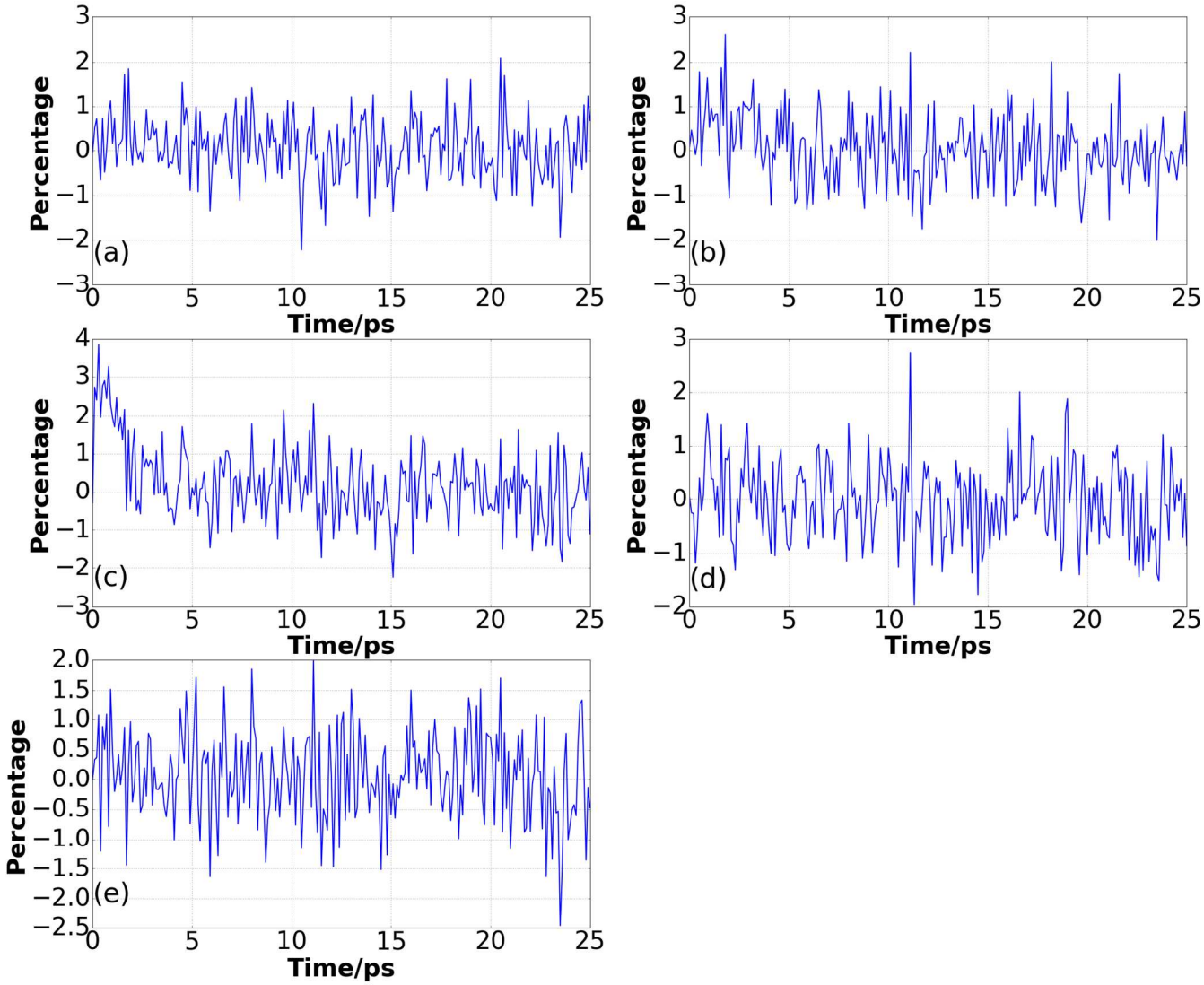

Fig. S25. Time-dependent percentage differences between the Eq-RMSDs and NEq-RMSDs of the vertical distance between the guanosine plane and the hydrogen atom in the second H-bond. The NEq-RMSDs are computed using the non-equilibrium ensembles produced by the initial vibrational excitation of (a) NM1; (b) NM2; (c) NM3; (d) NM4 and (e) NM5 in DMA-GC-Anth.

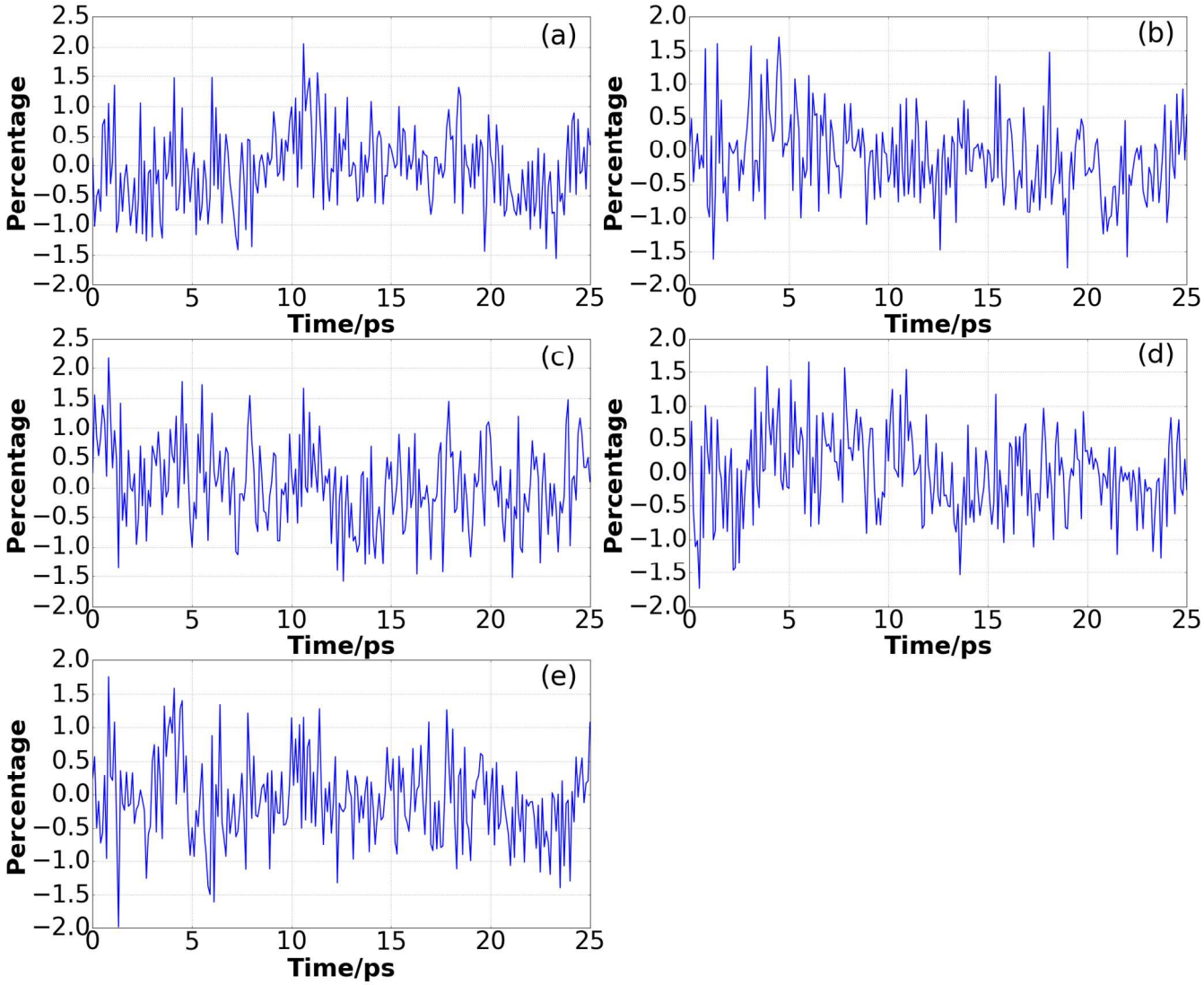

Fig. S26. Time-dependent percentage differences between the Eq-RMSDs and NEq-RMSDs of the vertical distance between the guanosine plane and the hydrogen atom in the third H-bond. The NEq-RMSDs are computed using the non-equilibrium ensemble produced by the initial vibrational excitation of (a) NM1; (b) NM2; (c) NM3; (d) NM4 and (e) NM5 in DMA-GC-Anth.

II.5 Distance and dihedral angle between donor (DMA) and acceptor (anthracene)

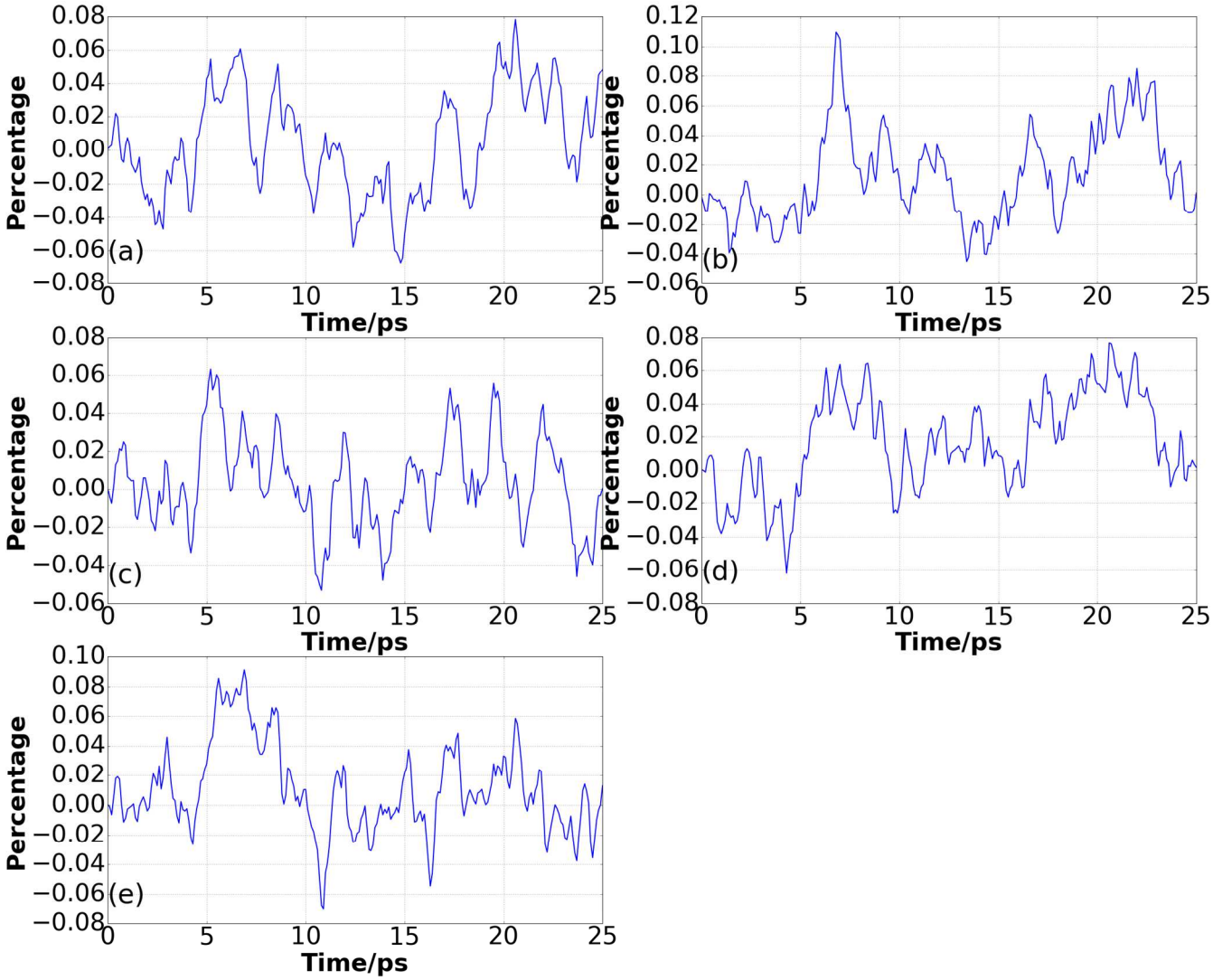

Fig. S27. Time-dependent percentage differences between the Eq-means and NEq-means of the D-A center-of-mass distance. The NEq-means are computed using the non-equilibrium ensembles produced by the initial vibrational excitation of (a) NM1; (b) NM2; (c) NM3; (d) NM4 and (e) NM5 in DMA-GC-Anth.

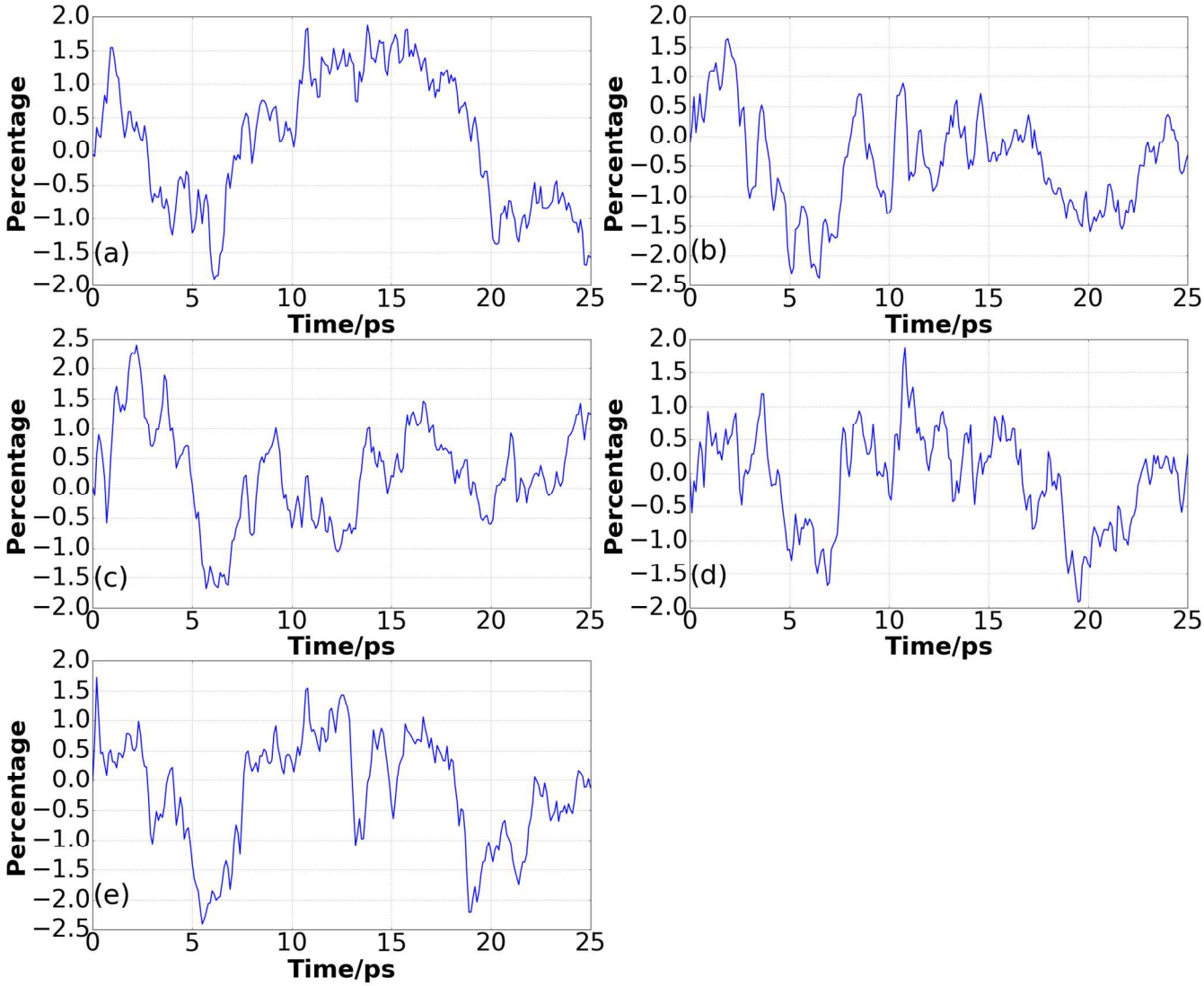

Fig. S28. Time-dependent percentage differences between the Eq-RMSDs and NEq-RMSDs of the D-A center-of-mass distance. The NEq-RMSDs are computed using the non-equilibrium ensembles produced by the initial vibrational excitation of (a) NM1; (b) NM2; (c) NM3; (d) NM4 and (e) NM5 in DMA-GC-Anth.

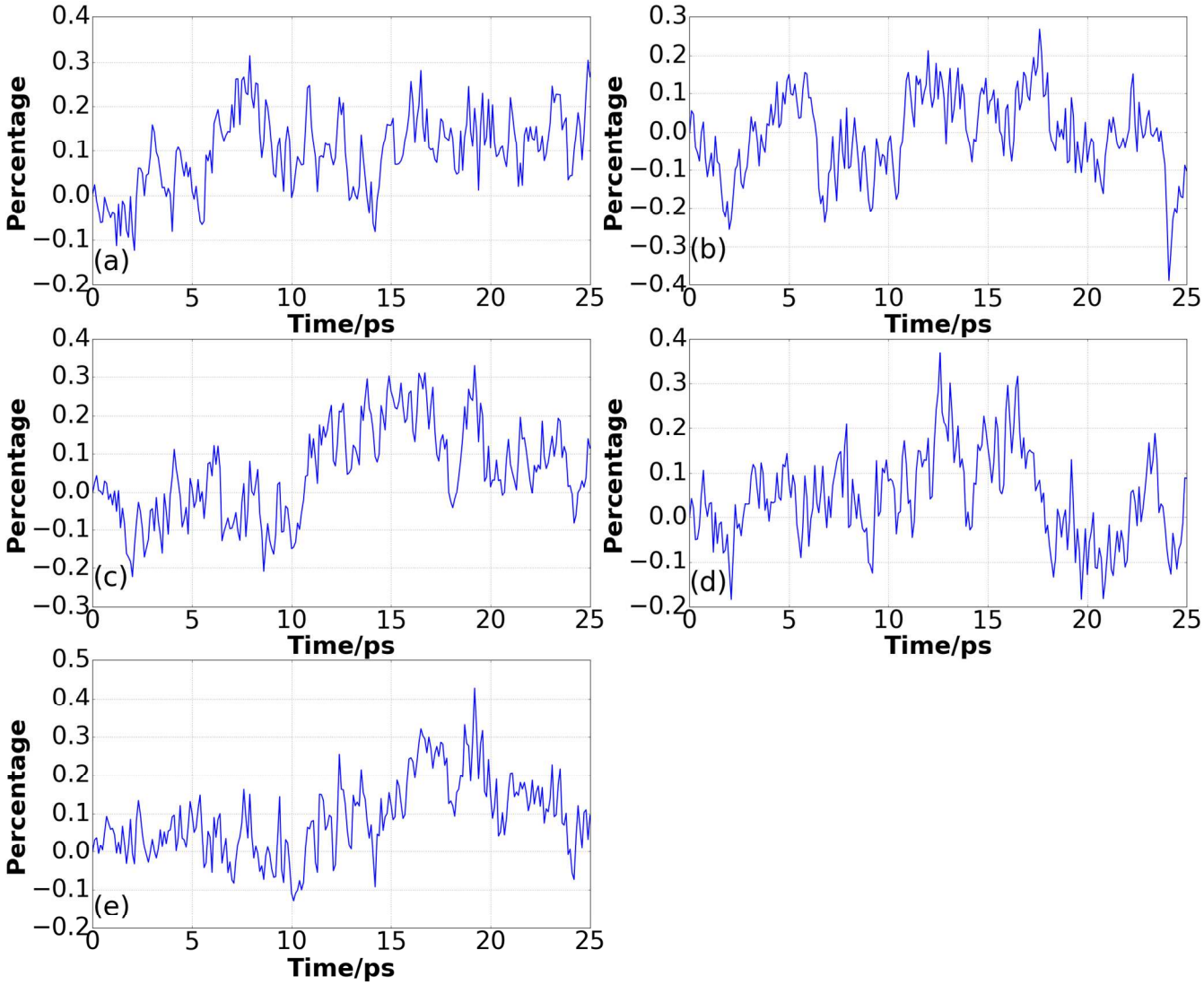

Fig. S29. Time-dependent percentage differences between the Eq-means and NEq-means of the D-A dihedral angle. The NEq-means are computed using the non-equilibrium ensembles produced by the initial vibrational excitation of (a) NM1; (b) NM2; (c) NM3; (d) NM4 and (e) NM5 in DMA-GC-Anth.

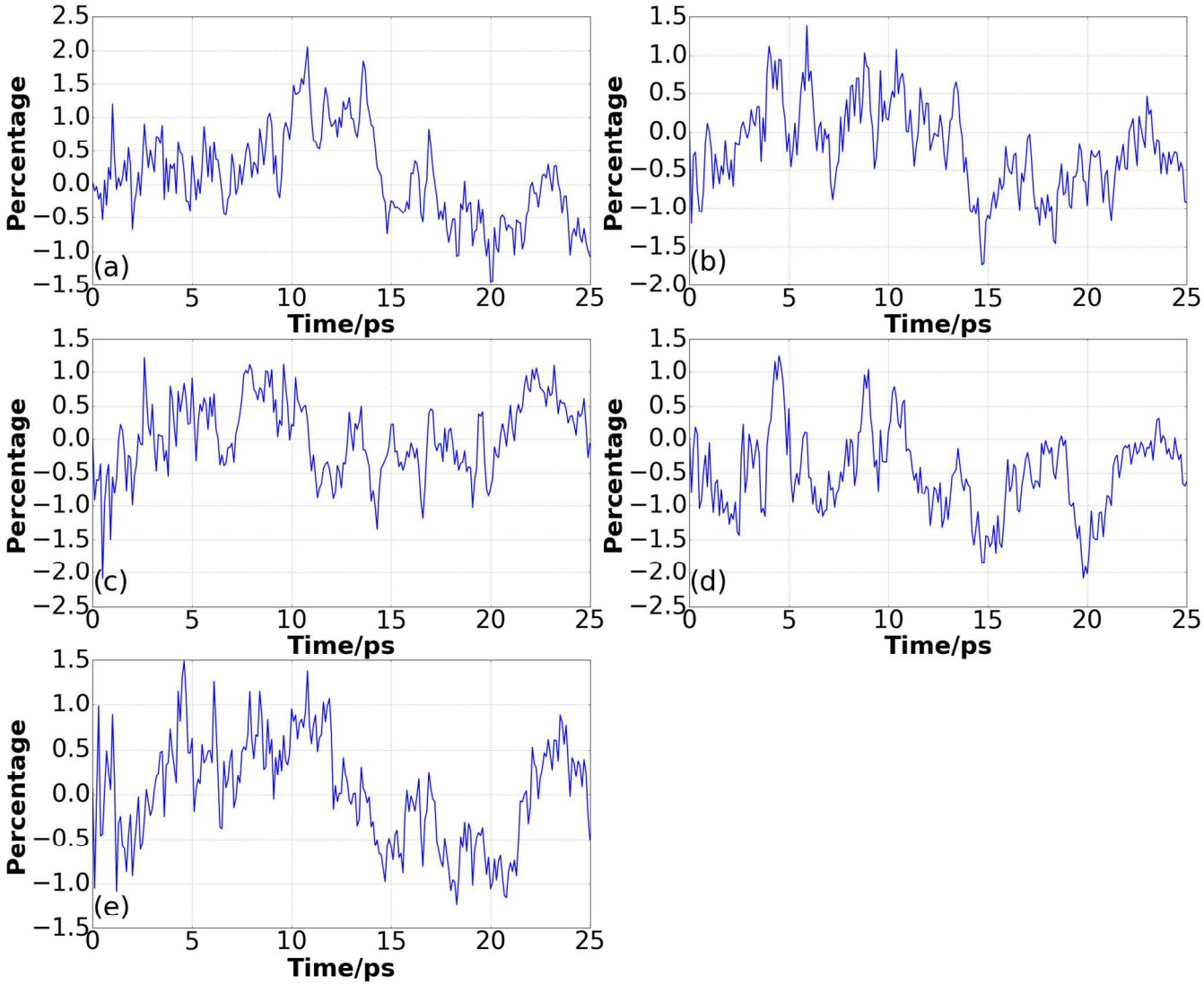

Fig. S30. Time-dependent percentage differences between the Eq-RMSDs and NEq-RMSDs of the D-A dihedral angle. The NEq-RMSDs are computed using the non-equilibrium ensembles produced by the initial vibrational excitation of (a) NM1; (b) NM2; (c) NM3; (d) NM4 and (e) NM5 in DMA-GC-Anth.

III. IR-induced electronic coupling perturbations in DMA-GC-Anth

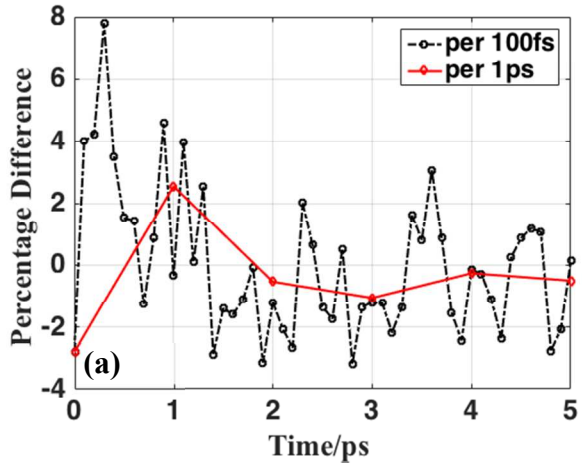

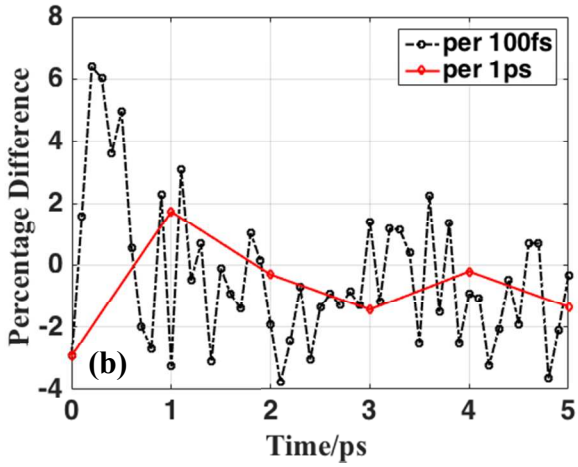

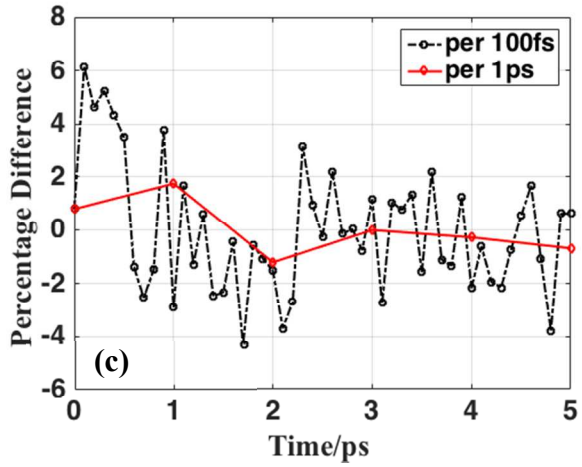

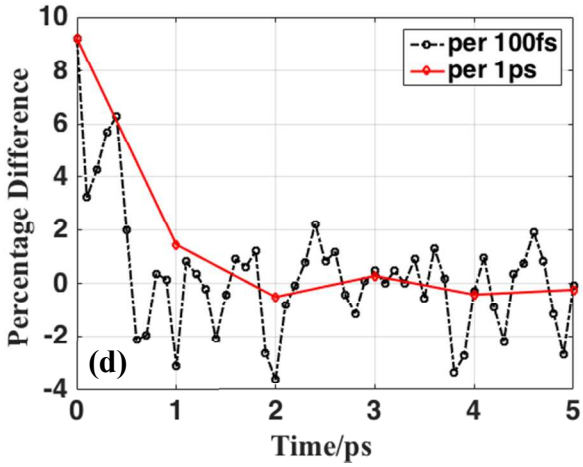

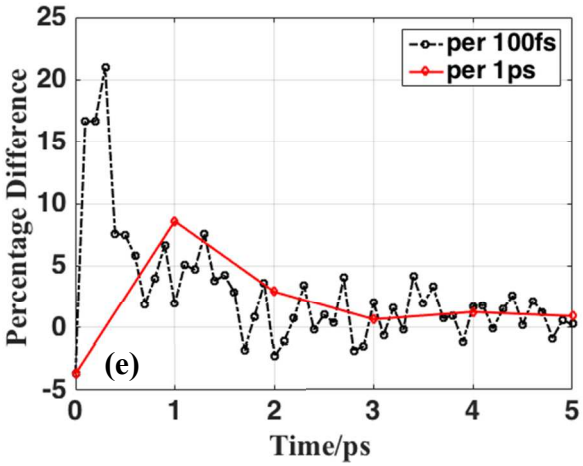

Fig. S31. Time-dependent percentage difference between the $\langle|H_{DA}|^2\rangle$ calculated from equilibrium ensemble and the $\langle|H_{DA}|^2\rangle$ calculated from non-equilibrium ensembles based on DFTB/3ob-3-1 description of electronic structure where mode (a) NM1; (b) NM2; (c) NM3; (d) NM4; (e) NM5 is excited at t=0ps. The percentage differences are presented at each 100fs time grid. The percentage differences between Eq- and NEq- averaged squared coupling within each 1ps window are also presented at each 1ps time grid.

IV. Application of NEqMD on ET reactions in PP-BCN-CA structure

IV.1 Time-dependent geometry analysis of PP-BCN-CA structure

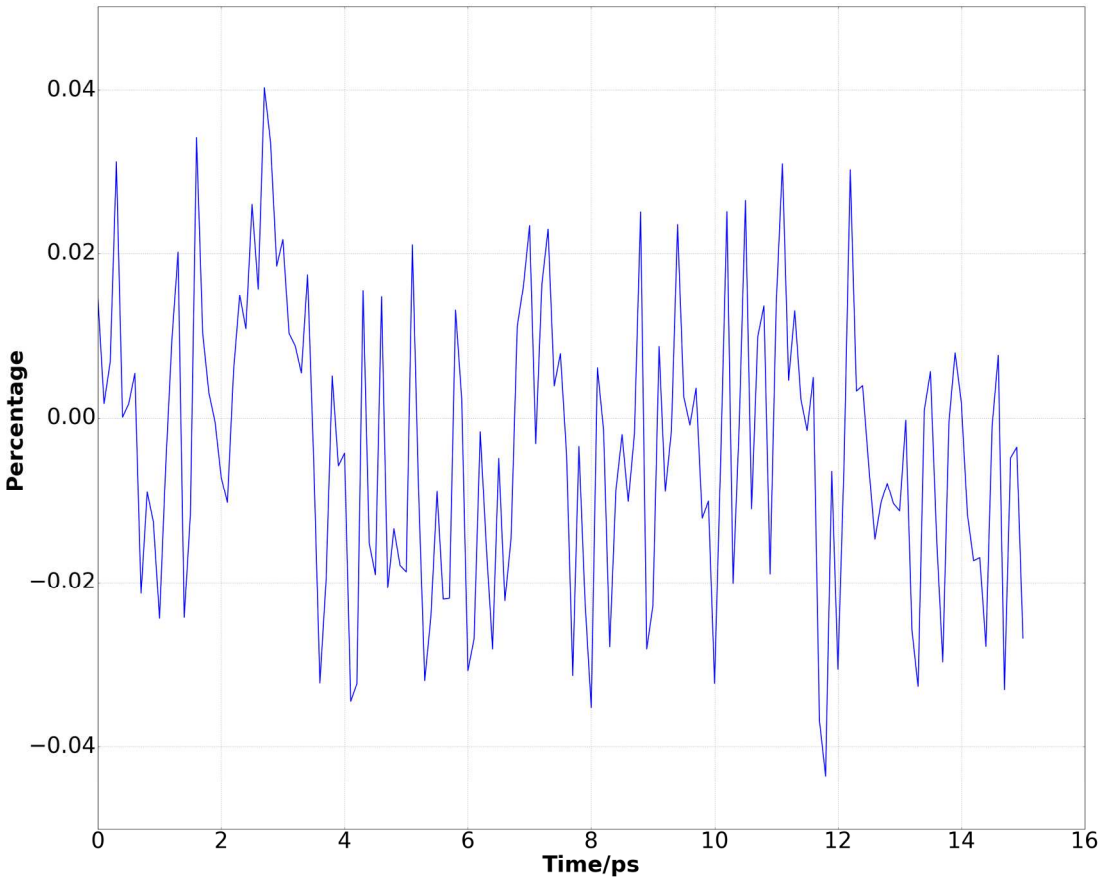

Fig. S32. Time-dependent percentage differences between the Eq-means and NEq- means of the donor-acceptor center-of-mass distance in PP-BCN-CA. The NEq- means are computed using the non-equilibrium ensembles produced by the initial vibrational excitation of NM6 of PP-BCN-CA.

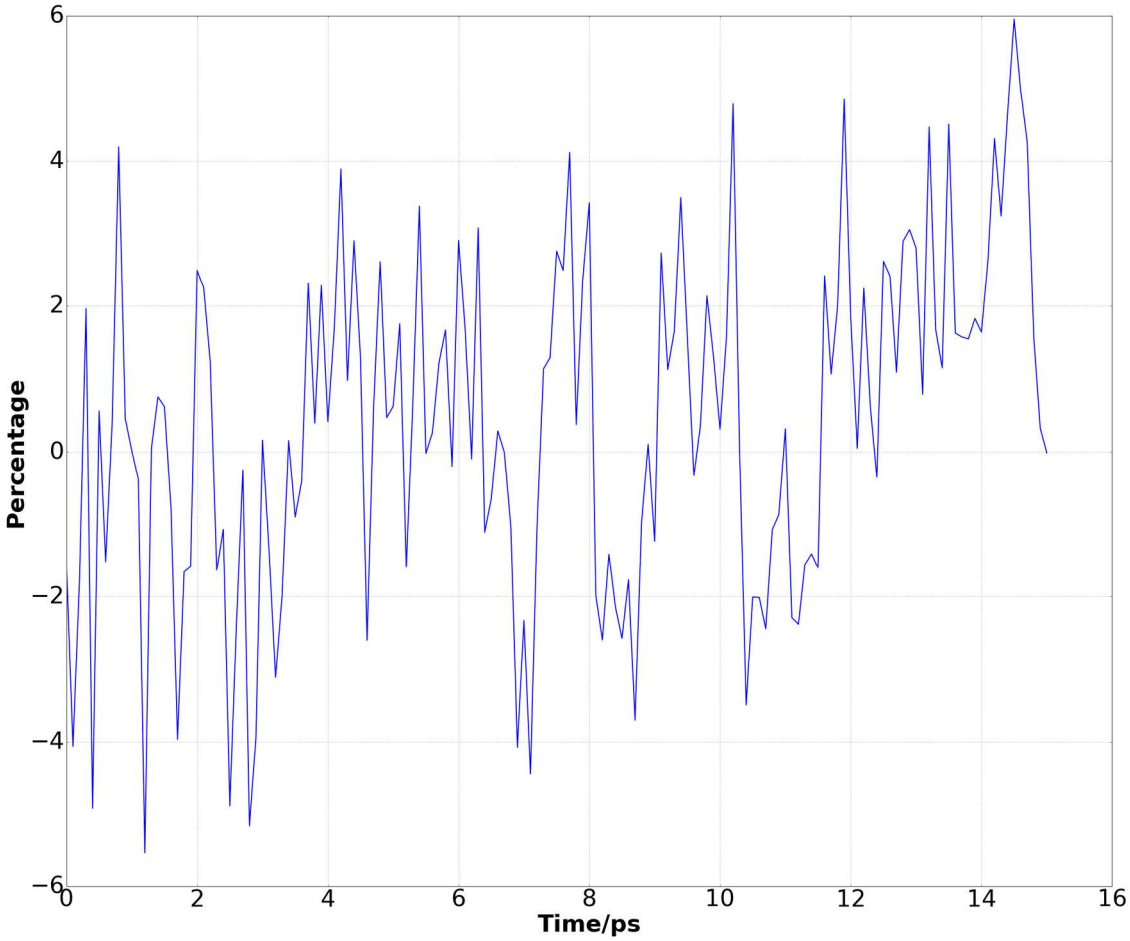

Fig. S33. Time-dependent percentage differences between the Eq-RMSDs and NEq-RMSDs of the donor-acceptor center-of-mass distance in PP-BCN-CA. The NEq-RMSDs are computed using the non-equilibrium ensembles produced by the initial vibrational excitation of NM6 of PP-BCN-CA.

IV.2 Dependence of charge-separation DA couplings and charge-recombination DA couplings on the normal coordinate of NM6 in PP-BCN-CA

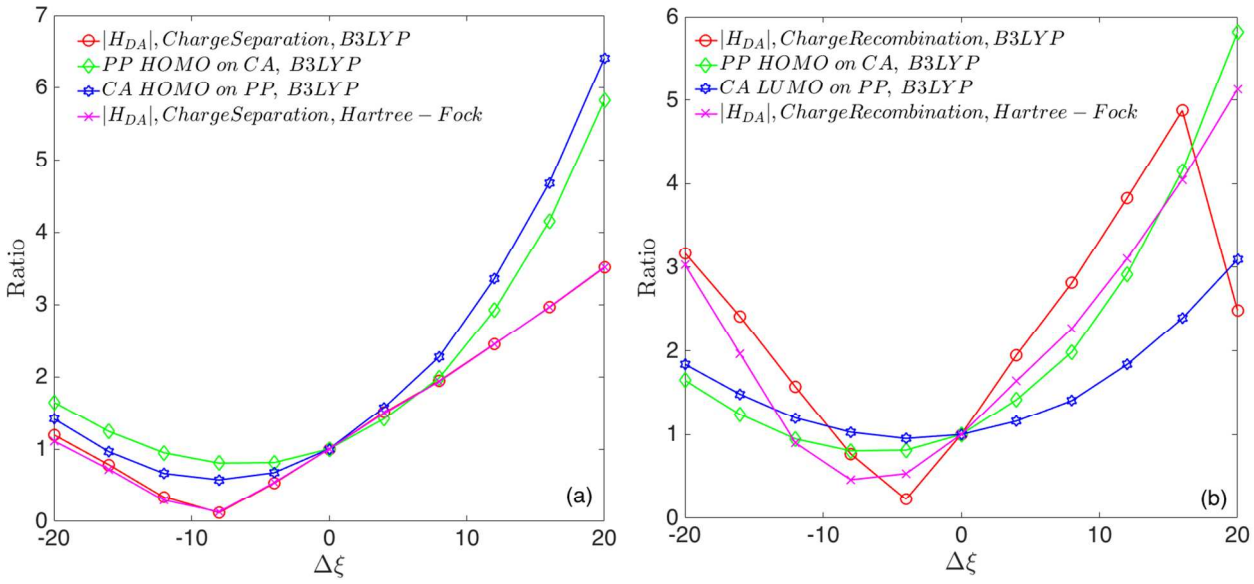

Fig. S34. Dependence of GMH-computed DA coupling of (a) charge separation; (b) charge recombination; and orbital delocalization on the normal mode coordinate of NM6 in PP-BCN-CA system. The electronic structure of PP-BCN-CA is calculated using B3LYP/6-31G(d, p) and Hartree-Fock/6-31G(d,p). The coupling values and MO amplitudes are all scaled by corresponding values at equilibrium position ($\Delta\xi = 0$). When the three C=N bond lengths decrease (positive $\Delta\xi$), both the amplitudes of PP HOMO on CA fragment and the amplitudes of CA HOMO on PP fragment increase. The behavior of orbital delocalization agrees well with the behavior of computed DA coupling. Both Hatree-Fock method and DFT/B3LYP give similar trend of the DA coupling along the normal mode coordinate of NM6.

References:

1. Skourtis, S. S.; Waldeck, D. H.; Beratan, D. N., Fluctuations in Biological and Bioinspired Electron-Transfer Reactions. *Annu. Rev. Phys. Chem.* **2010,** *61*, 461-485.

2. Skourtis, S. S.; Balabin, I. A.; Kawatsu, T.; Beratan, D. N., Protein Dynamics and Electron Transfer: Electronic Decoherence and Non-Condon Effects. *Proc. Natl. Acad. Sci. U.S.A.* **2005,** *102*, 3552-3557.